Tropical Anvil Clouds: Radiative Driving Towards a Preferred State

Adam B. Sokol[1], **Dennis L. Hartmann**[1]

[1]Department of Atmospheric Sciences, University of Washington, Seattle, WA, USA

Key Points:

- Radiative processes drive anvil clouds towards a favored structure at which they exert a positive cloud radiative effect
- Clouds prone to radiative destabilization have higher concentrations of ice crystals
- The properties of aged cirrus may depend on the time of day at which they were detrained

Corresponding author: Adam B. Sokol, `abs66@uw.edu`

Abstract

The evolution of anvil clouds detrained from deep convective systems has important implications for the tropical energy balance and is thought to be shaped by radiative heating. We use combined radar-lidar observations and a radiative transfer model to investigate the influence of radiative heating on anvil cloud altitude, thickness, and microphysical structure. We find that high clouds with an optical depth between 1 and 2 are prevalent in tropical convective regions and can persist far from any convective source. These clouds are generally located at higher altitudes than optically thicker clouds, experience strong radiative heating, and contain high concentrations of ice crystals indicative of turbulence. These findings support the hypothesis that anvil clouds are driven towards and maintained at a preferred optical thickness that corresponds to a positive cloud radiative effect. Comparison of daytime and nighttime observations suggests that anvil thinning proceeds more rapidly at night, when net radiative cooling promotes the sinking of cloud top. It is hypothesized that the properties of aged anvil clouds and their susceptibility to radiative destabilization are shaped by the time of day at which the cloud was detrained. These results underscore the importance of small-scale processes in determining the radiative effect of tropical convection.

Plain Language Summary

Clouds play an important role in Earth's energy balance, especially in the tropics. Thick clouds cool the climate by reflecting sunlight, while thinner clouds located high in the atmosphere warm the climate due to their strong greenhouse effect. Tropical thunderstorms generate expansive cloud systems ("anvil" clouds) that initially exert a cooling effect but evolve over time to produce a warming effect. Their net impact on the climate system depends on how much time they spend in their cooling and warming stages. In this study, we use satellite measurements and a radiation model to examine how anvil clouds evolve. We find that anvil clouds with a climate-warming effect are pervasive in the tropics and can be found far from any thunderstorm that would have produced them, suggesting that they are maintained in their warming stage for long periods of time. We observe some unique characteristics of these clouds that provide clues about the processes that maintain them. Our findings provide real-world support for previous hypotheses that, until now, relied on computer simulations. They also highlight the importance of small-scale processes in shaping the large-scale tropical energy balance and underscore the need to consider these processes in projections of future climate change.

1 Introduction

Convective clouds play an important role in the energy budget of the tropical atmosphere. Mesoscale convective systems (MCSs) consisting of deep, rainy convective cores and detrained anvil clouds reflect incoming shortwave (SW) radiation and trap outgoing longwave (LW) radiation emitted by Earth's surface and lower atmosphere. These SW and LW effects are individually strong but nearly cancel each other out on climatological scales. As a result, the net cloud radiative effect (NCRE) in tropical convective regions is near zero (Harrison et al., 1990; Ramanathan et al., 1989; Hartmann et al., 2001). Despite longstanding knowledge of this cancellation, questions remain about its very nature and susceptibility to change. There are compelling reasons to deepen our understanding of convection's radiative balance: changes to the balance would themselves constitute an important climate feedback (Hartmann, 2016) and could alter patterns in sea surface temperature (Wall et al., 2019), convective aggregation (Bretherton et al., 2005; Wing & Emanuel, 2014), and atmospheric circulation and precipitation (e.g., Randall et al., 1989; Voigt & Shaw, 2015),

The radiative neutrality of tropical convection owes itself to the widespread presence of moderately thick anvil clouds. These clouds exhibit a weakly positive NCRE but

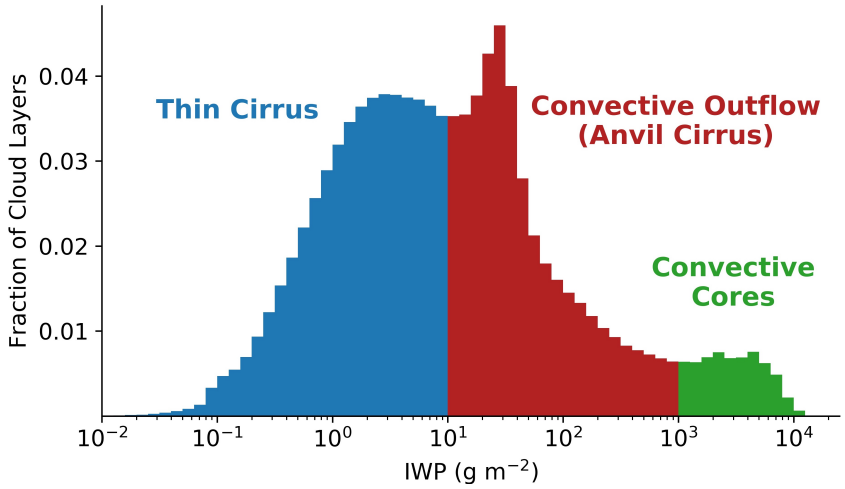

Figure 1. Histogram of cloud layer IWP for clouds with tops above 10 km in the tropical western Pacific (12°S-12°N, 150°E-180°E). Three cloud types are identified for heuristic purposes using the histogram's two relative minima as boundaries. Layer IWP is calculated using the DARDAR-CLOUD data set prior to the lidar sensitivity correction described in section 2.2. Bin widths are 0.1 in log space.

are long lasting and horizontally expansive, allowing them to balance the strongly negative NCRE exhibited by deep convective cores and optically thick anvil clouds over a smaller area (Hartmann & Berry, 2017). The pervasiveness of moderately thick anvils is evident in the observed distribution of ice water path (IWP) of high cloud layers over the western Pacific warm pool (Figure 1). The distribution suggests three cloud layer categories: deep convective cores, convective outflow (anvil cirrus), and thin cirrus that are characteristic of the tropical tropopause layer. The monotonic increase in frequency as IWP decreases from 10^3 to $\sim$30 g m^{-2} represents the flattening and horizontal spreading of anvil clouds after they are detrained (Lilly, 1988). The distribution peaks at $\sim$30 g m^{-2} before falling and rising again to the in situ mode at $\sim$2 g m^{-2}. This bimodality suggests that anvil clouds do not simply continue to thin and spread once their IWP reaches the anvil modal value. If that were the case, one would expect to observe a continuous trajectory between deep convective cores and the lowest observable IWP. Distinct anvil and thin cirrus modes have previously been observed in the Southeast Asian monsoon region (Berry & Mace, 2014), but the causes of bimodality remain largely unexplored. To understand how the anvil cloud distribution may change in the future, it is necessary to understand the processes that govern the evolution of convective outflow.

Radiative heating has long been recognized as an important driver of anvil cloud dynamics (Lilly, 1988; Ackerman et al., 1988). Optically thick anvil clouds undergo strong LW heating near cloud base and cooling at cloud top, which leads to destabilization and in-cloud convective mixing (Dobbie & Jonas, 2001; Schmidt & Garrett, 2013). Solar heating of cloud top during the day works against this destabilization but is generally weaker in magnitude than LW heating (Ackerman et al., 1988). Optically thin cirrus are heated throughout by both LW and SW; this generates buoyancy and drives a mesoscale circulation that lofts the cloud with respect to its clear-sky surroundings and promotes its horizontal spreading. The importance of radiatively driven motions in the anvil cloud life cycle is supported by cloud-resolving model simulations showing that anvil lifetimes are substantially prolonged by radiative heating (Dobbie & Jonas, 2001; Hartmann et al., 2018; Gasparini et al., 2019). However, the relative importance of in-cloud convection and mesoscale lofting remains unclear. Others have suggested that anvil cloud per-

sistence results not from radiative heating but from the slow pace of ice crystal evaporation in the cold upper troposphere (Seeley et al., 2019).

Recent work has helped to better understand the connections between radiative heating, anvil cloud evolution, and the climatological NCRE of tropical convection. Hartmann and Berry (2017) hypothesized that radiative heating plays a critical role in driving the convective cloud population towards one that results in the observed near-neutral NCRE. Their hypothesis, which we refer to as the selective cloud maintenance hypothesis, posits that the LW heating dipole in optically thick anvil clouds acts to thin them until the vertical gradient in cloud radiative heating is strong enough to incite in-cloud convection, which maintains the cloud at an optical thickness corresponding to a positive NCRE. This maintenance of positive-NCRE anvils balances the negative NCRE exhibited during the earlier stages of the MCS life cycle. The selective cloud maintenance hypothesis was further explored by Hartmann et al. (2018), who found that radiatively driven turbulence maintains moderately thick anvil clouds by vertically recycling water vapor. In-cloud updrafts promote ice growth by vapor deposition, drive new ice crystal nucleation, and counteract sedimentation. The water vapor supply is then replenished by the sublimation of ice crystals in descending air parcels. The strength of this "microphysical cycling" mechanism is sensitive to changes in the model microphysical scheme, and the importance of fresh ice crystal nucleation is particularly unclear. Other simulations have found nucleation to play a lesser role in cloud maintenance (Gasparini et al., 2019), and aircraft measurements of anvil clouds in the eastern Pacific found only a handful of cases in which ice crystal concentrations were reflective of nucleation events (Jensen et al., 2009).

The selective cloud maintenance hypothesis and microphysical cycling mechanism have yet to be validated by observations. Previous observational studies have used geostationary satellite measurements to track the radiative evolution of individual MCSs (Wall et al., 2018) and spaceborne radar retrievals to examine anvil vertical structure (Yuan et al., 2011). In both of these studies, instrumental limitations prevented the detection of certain cloud properties that are important to the evaluation of anvil cloud maintenance mechanisms. In situ observations (e.g., Heymsfield et al., 2002; Jensen et al., 2009) have provided important insights into anvil cloud vertical structure but are limited in amount and scope.

The objective of this study is to characterize the microphysical and macrophysical evolution of tropical anvil clouds using the observational tools necessary to capture their entire life cycle. In doing so, we evaluate the selective cloud maintenance hypothesis, the relative importance SW and LW radiative heating, and the plausibility of microphysical cycling. Observational data are described in section 2. In section 3, we describe our methods for identifying anvil clouds and deep convective cores and for calculating radiative heating rates. Distributions of anvil clouds and their optical properties are presented in sections 4.1 and 4.2, respectively, and their evolution is discussed in sections 4.3 and 4.4. We summarize our findings and discuss their implications in section 5.

2 Satellite Data

We use observations from several instruments aboard satellites belonging to the A-train constellation (Stephens et al., 2002). The A-train follows a sun-synchronous orbit that crosses the equator at approximately 01:30 and 13:30 local time (which we also refer to as night and day, respectively). This allows for the comparison of daytime and nighttime cloud populations but precludes the study of how individual anvil clouds evolve over time. Geostationary satellite measurements have been used in the past to examine the MCS life cycle (Wall et al., 2018), but these passive sensors fail to capture optically thin anvil clouds and cannot provide information about vertical structure, both of which are

necessary to evaluate anvil maintenance processes. We use combined radar-lidar retrieval products to identify anvil clouds and examine their microphysical structure. Deep convective cores are identified using coincident observations of brightness temperature within the atmospheric window. This section provides a description of these datasets and of the study domain.

2.1 Combined Radar-Lidar Retrievals

The A-train constellation hosts the Cloud-Aerosol Lidar and Infrared Pathfinder Satellite Observations (CALIOP) instrument aboard the CALIPSO satellite and the Cloud Profiling Radar aboard the CloudSat satellite. Berry and Mace (2014) demonstrated that both instruments are needed to detect the full spectrum of radiatively active cirrus in tropical convective regions. The sensitivity of CALIOP to small ice crystals allows it to detect thin cirrus clouds and the tenuous tops of thicker cloud layers. However, because the lidar signal becomes fully attenuated at an optical depth of 4-5, it is unable to capture the full extent of optically thick clouds (Winker et al., 2010). Those clouds are better captured by the CloudSat radar's longer wavelength, which is sensitive to large ice crystals but does not detect the smaller ones seen by CALIOP. The coincident radar and lidar observations offered by the A-train constellation can thus be synergistically used to detect cloudy volumes with a wide range of optical properties.

We obtain combined CloudSat-CALIPSO observations from two DARDAR (raDARliDAR) data products. As described in Delanoë and Hogan (2008), the DARDAR algorithm combines CALIOP and CPR measurements using a variational scheme that estimates ice cloud properties for cloudy volumes detected by both instruments and for those detected by only one instrument. When both instrument are available, two independent pieces of information are known about the cloud particle size distribution, which allows the retrieval to rely less on empirical, a priori estimates than it does for regions detected by only one instrument. The DARDAR grid has a vertical resolution of 60 m and ∼1.1-km horizontal spacing between profiles.

Cloud layer information and ice microphysical properties are obtained from DARDAR-CLOUD v2.1.1 (Delanoë & Hogan, 2010). DARDAR-CLOUD uses a vertical separation threshold of 480 m to identify cloud layer and provides profiles of retrieved visible extinction coefficient (α_v), ice water content (IWC), and effective radius (r_e). We further calculate the visible optical depth (τ) and IWP of each cloud layer by vertically integrating α_v and IWC, respectively. DARDAR-CLOUD has been extensively used and evaluated against in situ observations and other combined retrieval products (e.g., Deng et al., 2013; Stein et al., 2011; Delanoë et al., 2013). Nevertheless, the errors associated with the retrieval algorithm are substantial, and several shortcomings in the DARDAR-CLOUD version used here have been identified. The most relevant shortcoming to this study is the apparent overestimation of α_v and IWC in regions seen by the lidar alone (Deng et al., 2013), which implies that the cloud layer τ and IWP calculated in the present study may be biased high in some cases. For a more detailed discussion of the errors associated with DARDAR-CLOUD and the improvements made to reduce them, we direct the reader to Delanoë and Hogan (2010) and Cazenave et al. (2019).

In addition to the DARDAR-CLOUD retrievals, we obtain estimates of ice crystal number concentration from DARDAR-NICE v1.0 (Sourdeval et al., 2018). We use the DARDAR-NICE retrieval of the concentration of ice crystals with a maximum diameter greater than 5 μm (N_i). The N_i estimation methodology assumes a monomodal particle size distribution and is suited for temperatures below -30°C, since the presence of supercooled liquid becomes increasingly likely at higher temperatures. This study focuses primarily on anvil clouds colder than -30°C, so we do not expect the increased uncertainty at higher temperatures to interfere with out results. DARDAR-NICE is difficult to validate on a large scale due to the lack of other global, long-term number con-

centration datasets. Nevertheless, Sourdeval et al. (2018) found it to agree reasonably well with coincident aircraft observations and provide a detailed discussion of retrieval accuracy.

2.2 Correcting for the Diurnal Cycle of Lidar Sensitivity

Because we seek to compare daytime (13:30 LT) and nighttime (01:30 LT) observations of anvil clouds, differences in instrument sensitivity during day and night must be taken into account. The CALIOP minimum detectable backscatter is highest during the day due to background solar noise (McGill et al., 2007), which prevents the detection of tenuous cloud features that would otherwise be detected at night. This difference can be seen in Figure 2, which shows daytime and nighttime histograms of DARDAR-CLOUD α_v for pixels seen by the lidar only. The diurnal cycle of lidar sensitivity is apparent at low values of α_v, which are detected frequently at 01:30 but rarely at 13:30. The histograms show much better agreement for values of α_v exceeding the daytime modal value, which suggests a reduced impact of solar noise. Low-extinction pixels are often found at cloud edge, which complicates the comparison of 01:30 and 13:30 cloud geometries. To account for this, we remove all cloudy, lidar-only pixels from the DARDAR retrievals for which α_v is less than 0.12 km^{-1} and treat them as if they are clear sky. The threshold corresponds to the daytime modal value and is indicated by the dashed black line in Figure 2). The correction removes 21.5% of daytime lidar-only pixels and 49.0% of nighttime lidar-only pixels, which has important implications for the detection of properties such as cloud top height and geometric thickness. On average, cloud layer top height is reduced by 126 and 333 m during day and night, respectively. Despite this, the impact of the correction on cloud layer τ is negligible, since the affected pixels contribute relatively little to the layer-integrated α_v. The implications of the correction on cloud fraction statistics are discussed in section 4.1.

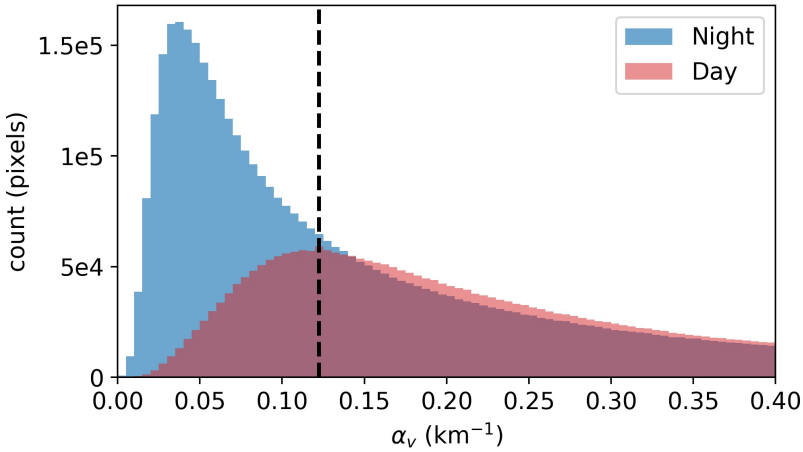

Figure 2. Histograms of visible extinction coefficient, α_v, for DARDAR-CLOUD lidar-only pixels during the 13:30 (day; blue) and 01:30 (night; red) equatorial crossings. The vertical dashed line represents the threshold used to correct for the diurnal variation in lidar sensitivity. Data from the full month of May, 2009, from the two study regions described in section 2.4 are used.

2.3 MODIS brightness temperature

Observations of 11-μm brightness temperature (TB_{11}) are provided by the Moderate Resolution Imaging Spectroradiometer (MODIS) aboard the Aqua satellite. MODIS is a scanning radiometer that provides plan view observations coincident with CloudSat and CALIPSO measurements. Because the cloud-free atmosphere is nearly transparent to infrared radiation in the 11-μm band, the TB_{11} measured from space is sensitive to the presence of optically thick clouds with cold tops and can be used to detect deep convective cores. Here, we obtain TB_{11} (MODIS channel 31) from the Level 2 Cloud Product (Platnick et al., 2017). Each MODIS data granule has a swath width of 2,330 km and includes 5 minutes of observations, corresponding to an along-track length of about $\sim$2,000 km. TB_{11} measurements are provided at 5$\times$5 km resolution. Our method for identifying deep convective cores from these observations is described in section 3.2.

2.4 Study Domain

We use observations from two tropical maritime regions extending from 12°S to 12°N: the Indian Ocean (IO; 55°E-95°E) and the West Pacific (WP; 150°E-180°E). These two regions both have a small climatological NCRE despite frequent deep convection (Ramanathan et al., 1989; Harrison et al., 1990). Furthermore, MCSs in both regions tend to be aggregated into large complexes consisting of several convective cores with connected anvil cloud decks (Yuan & Houze, 2010). This stands in contrast to the nearby Maritime Continent region, in which MCSs are frequent and extensive but tend to be separated from one another. In order to restrict our analysis to maritime convection, we exclude observations from the southern tip of the Indian subcontinent that falls within the bounding box of the IO region. We use all DARDAR and MODIS observations available from the two study regions for the 2009 calendar year. This amounts to over 4.2 million DARDAR retrieval profiles (57.3% from IO; 42.7% from WP), which are about evenly split between night and day. Data is unavailable between 16 Feb. and 12 March and between 8 Dec. and 31 Dec.

3 Methods

This section describes how anvil cloud layers and deep convective cores are identified from DARDAR and MODIS observations, respectively. We then describe our representation of anvil cloud evolution and our method of calculating radiative heating rates.

3.1 Anvil Identification

For the purposes of this paper, we use the term "anvil cloud" to refer to high ice cloud layers that are likely produced by deep convection. We search each DARDAR vertical profile for anvil cloud layers after its low-extinction pixels have been removed as described in section 2.2. The uppermost four cloud layers in each profile are identified using the DARDAR cloud layer index and are each evaluated against three criteria, all of which must be met for the layer to be considered an anvil layer. First, the layer must have a cloud top height (CTH) above 10 km. This excludes mid-level convection from our analysis and corresponds to the minimum CTH used by Berry and Mace (2014) in their definitions of cirrus layers. Second, the layer must have a cloud base height (CBH) above 5 km, which corresponds to the average freezing level in the study regions as calculated from reanalysis temperature from the European Centre for Medium-Range Weather Forecasts, which is included in DARDAR-CLOUD. This criterion is intended to exclude deep convective cores, which have cloud bases near the surface. Lastly, the layer must have an IWP greater than 10 g m^{-2}. This threshold corresponds to the relative minimum between the two cirrus modes of the layer IWP distribution (Figure 1), and we therefore expect that it carries physical meaning. Of course, it is possible that some thin, liquid-

origin cirrus layers are wrongly excluded by this criterion and that some thick, in situ-formed cirrus are wrongly included, but we expect these cases to be small in number compared to our sample size.

If multiple cloud layers in a single profile meet the three anvil criteria, the uppermost layer is included in our analysis and the lower anvil layers are discarded. Anvil layers lying below non-anvil cirrus layers are included. The limitation of our anvil cloud search to the uppermost four layers in each DARDAR profile is arbitrary but should have little effect on our results, since less than 0.2% of profiles contain more than four layers. The lidar sensitivity correction described in section 2.2 has minor effects on anvil identification. The correction results in the disqualification of 1.2% and 3.9% of daytime and nighttime cloud layers, respectively, that would have otherwise been classified as anvil clouds.

The results of the anvil identification methodology for a typical scene are shown in Figure 3a. This example demonstrates the ability of our three criteria to distinguish cirrus layers connected to deep convection from thin cirrus of unknown origin, such as the uppermost cloud layer present in the right-hand half of the scene. Several limitations

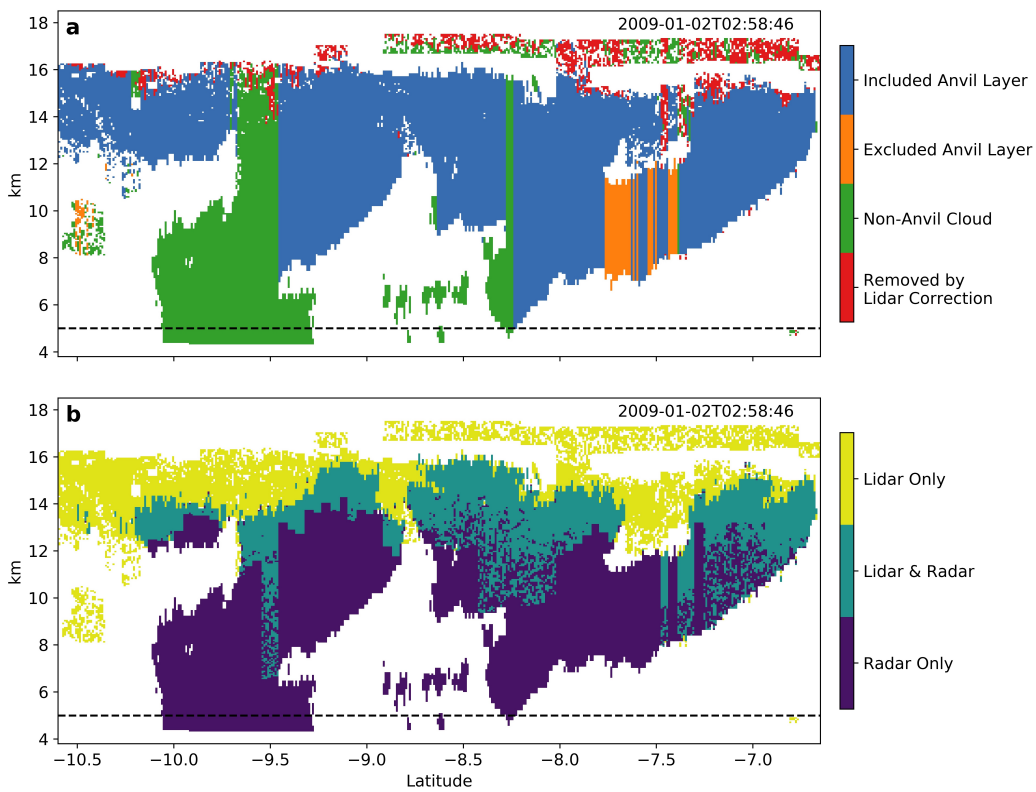

Figure 3. Example DARDAR-CLOUD scene from the West Pacific region. (a) Results of our anvil identification algorithm showing (blue) anvil cloud layers included in our analysis, (orange) anvil layers excluded from analysis because they are not the uppermost anvil layer in the column, (green) non-anvil layers, and (red) cloudy pixels that did not meet the minimum extinction threshold required by the lidar sensitivity correction. (b) Availability of lidar and radar measurements for the same scene. The dashed black line at the 5-km level indicates the minimum cloud base height permitted for anvil layers.

of our anvil identification methodology are also apparent. For example, different portions of the same anvil cloud formation can be included or excluded from our analysis depending on the characteristics of an overlying cloud layer. This can be seen between 7.3 and 7.8 °S, where a cloud-free gap centered at 12 km separates upper and lower prongs of the same cloud formation. In some profiles, the upper and lower prongs have enough vertical separation that they are considered distinct layers, and the lower layer is excluded from analysis if the upper layer qualifies as an anvil. In other profiles, the vertical separation is small enough that the two prongs are considered to be a single anvil layer. Because our anvil identification methodology considers each profile individually, it cannot account for nuances such as these that are apparent when the profile is viewed within its larger context. We have inspected more cloud scenes and found that scenarios such as the one discussed here are rare, and we do not expect this limitation to have significant impacts on our results.

The ability of the CALIPSO lidar and CloudSat radar to detect different portions of clouds is demonstrated in Figure 3b. It is clear even from this one example that both instruments are needed to detect anvil clouds and to accurately determine properties such as CTH and geometric thickness. While most of the anvil layers shown in this particular example include observations from both instruments, some thin anvil layers (such as those on the left-hand edge of the scene) would go entirely undetected if the radar alone was relied upon. This supports the conclusion of Berry and Mace (2014) that both instruments are needed to capture the full spectrum of radiatively active ice clouds. Of all anvil layers identified in this study, 72.1% are detected by both instruments (though not necessarily at the same altitude), 27.6% are detected by only the lidar, and 0.3% are detected by only the radar.

3.2 Convective Core Identification

Once anvil cloud layers were identified, we used MODIS TB_{11} observations to find the spreading distance of each anvil observation from the nearest deep convective core (d_{core}). Different methods of convective core identification using infrared brightness temperature measurements have been demonstrated and discussed in the literature (e.g., Gettelman et al., 2002; Setvák et al., 2006; Young et al., 2012). Here, we use a simple TB_{11} threshold of 210 K. For each segment of the CloudSat-CALIPSO orbit that passes through the study region, we stitch together all corresponding MODIS granules to construct a single, plan view TB_{11} swath. We then identify contiguous clusters of pixels with TB_{11} below 210 K. Pixels that share a corner are considered contiguous, and any cluster that contains two or more pixels with $TB_{11} < 210$ K is considered to be a convective core. Spreading distance is then calculated, and the MODIS TB_{11} at the location of the DARDAR profile is found using nearest-neighbor interpolation. When the CloudSat-CALIPSO track is close to but within a study region boundary, the corresponding MODIS granules extend beyond the boundary and the nearest convective core may lie outside the study region. This was the case for ∼10% of anvil profiles, and the d_{core} measurements in these cases were considered valid. Our results are not sensitive to whether or not these cases are included. In rare cases, an anvil profile is closer to the edge of its corresponding MODIS granule than it is to the nearest core; the d_{core} measurements for these profiles are considered invalid and are not included in analysis. An important note about our convective core identification method is that it calculates the distance between each anvil profile and the nearest 210-K core without verification that the two features belong to the same MCS. Cirrus systems generated by deep convection can persist for much longer than the convection itself (Luo & Rossow, 2004), and the mechanisms of this persistence are exactly what we seek to explore. The presence of anvil clouds at great distances from active convection would offer evidence for anvil maintenance, and we therefore do not limit our analysis to anvil profiles that are immediately connected to an MCS.

Our method of convective core identification is susceptible to two types of errors. First, as demonstrated in Young et al. (2012), optically thick anvil clouds can be mistakenly classified as convective core when a 210-K TB_{11} threshold is used. Of the anvil cloud layers identified in the present study, 1.9% have interpolated MODIS TB_{11} below 210 K. Most of these anvil layers are optically thick, which suggests they are freshly detrained and located close to a convective core. This type of error would therefore increase the apparent size of a convective core by mistakenly including some of the surrounding anvil, which would result in artificially low d_{core} values for the anvil observations associated with that core. The second type of error that could occur is the failure to detect deep convective towers that do not reach sufficiently cold temperatures. This type of error would artificially reduce the frequency of deep convection, and, as a result, some anvil clouds may mistakenly appear to be very far from a convective core. We inspected the d_{core} values assigned to anvil layers thicker than the 95th percentile of geometric thickness (7.74 km), which are likely to be freshly detrained and close to their convective source. Approximately one fourth of these anvil layers are found to be more than 100 km away from the nearest core using our method. This shows that a non-negligible amount of convective cores may go undetected by a 210-K threshold, which is consistent with previous findings (Young et al., 2012).

While the convective core identification described here is relatively crude, it is sufficient for our purposes. The identification of convective cores in this study serves mainly to demonstrate that radiatively active anvil clouds can routinely be found far away from a convective source. Errors in d_{core} values on the order of tens of kilometers are inconsequential for these purposes, since MCSs can extend horizontally for hundreds of kilometers. Detailed analyses of MCS structure require a more refined method of core identification such as those used by (Yuan & Houze, 2010) and (Igel et al., 2014).

3.3 Representation of Anvil Evolution

Because radiative heating is central to the hypotheses we seek to evaluate and is closely tied to cloud optical thickness, we choose to use τ as an evolutionary coordinate. Anvil τ generally decreases with time after detrainment due to horizontal spreading, precipitation, and ice crystal sedimentation. Anvil profiles are binned by $\log_{10}\tau$ using a bin width of 0.1, and statistics are calculated for each bin.

There are two important things to keep in mind when interpreting how cloud properties vary with τ. First, the initial τ of freshly detrained anvils likely varies from storm to storm and may decrease rapidly if an anvil is still precipitating. It is therefore possible that an optically thinner anvil was detrained more recently than an optically thicker one detected at the same moment in time. Second, it should be remembered that the typical lifetime of detrained cirrus is comparable to the 12 hours between the 01:30 and 13:30 A-train equatorial crossings. Luo and Rossow (2004) found that cirrus systems associated with deep convection typically last for 19-30 ($\pm$16) hours, with the maximum cirrus amount occurring $\sim$12 hours after convection ceases (see their Figure 8). It is then likely that many of the optically thin cirrus detected during the day were detrained during the preceding night, and vice versa. This is particularly important for our comparison of 13:30 and 01:30 observations and our evaluation of diurnal differences in anvil cloud evolution. For both of these reasons, it should be remembered that the composites presented here simply reflect the observed anvil cloud population at the time of the two A-train equatorial crossings and are not necessarily representative of how individual cirrus systems evolve over time.

3.4 Radiative Heating Calculations

Anvil radiative heating rates are calculated using the single-column rapid radiative transfer model for general circulation modeling (RRTMG; Mlawer et al., 1997; Ia-

cono et al., 2000). Treatment of ice clouds follows Fu et al. (1998) and requires the specification of IWC and r_e. The ice particle size distribution has been found to vary vertically throughout anvil clouds in a characteristic way (Yuan et al., 2011; Heymsfield et al., 2002); averaging together anvil microphysics profiles from different altitudes would smear out much of this structure and have an effect on the calculated radiative heating rates. To avoid this, we construct representative IWC and r_e profiles for each τ bin to feed into the radiation code using the following procedure. Anvil profiles that have CTH within 500 m of the τ bin median are selected. The median CBH of that subset is calculated, and only those profiles with CBH within 500 m of the median are kept. The median IWC and r_e are found for each vertical level between the median CTH and CBH and are interpolated onto the RRTMG grid, which has a vertical resolution of 500 m. The resulting profiles have retained the altitude, geometric thickness, and microphysical structure characteristic of observed anvil clouds with similar τ. These profiles are generated separately for the 01:30 and 13:30 overpasses and for each of the two study regions. They are then fed into RRTMG, and heating rates are calculated using a surface temperature of 28 °C, a surface albedo of 0.08, 400 ppm CO_2, and average temperature, water vapor, and ozone profiles for the study region as calculated from 1989-2007 ERA-Interim reanalysis. For the 13:30 anvil profiles, we use an insolation of 1,261 W m^{-2}, which corresponds to equatorial insolation at 13:30 LT on the equinox. The model returns separate SW and LW heating rate profiles. The net heating rate, Q_R, is equal to the sum of the SW and LW heating rates for the 13:30 observations and is simply equal to the LW heating rate for the 01:30 observations.

We use the radiative heating model output profiles to compute two useful diagnostics. First, we calculate the mass-averaged radiative heating rate throughout the cloud layer, $\overline{Q}_R$, which can help understand the potential for mesoscale vertical lofting of the anvil with respect to its clear-sky surroundings. Second, we calculate the mass-averaged, in-cloud lapse rate tendency (LRT) due to radiative heating:

$$\left.\frac{\partial \Gamma}{\partial t}\right|_{rad} = -\frac{1}{P_B - P_T}\int_{P_T}^{P_B} \frac{\partial Q_R}{\partial z} dP \tag{1}$$

where Γ is the lapse rate, and P_B and P_T are the pressures at cloud base and cloud top, respectively. Positive LRT indicates a decrease in radiative heating with altitude, which destabilizes the vertical column. Negative LRT indicates increasing stabilization.

4 Results

We begin by discussing the results of our anvil cloud identification scheme in section 4.1. We then examine the distribution of anvil τ and how it changes with spreading distance in section 4.2. In section 4.3, we show how cloud macrophysical properties and radiative heating rates evolve with optical thinning and discuss how this evolution differs between day and night. Anvil cloud microphysical structure and its evolution are discussed in section 4.4.

4.1 Anvil Cloud Fraction

The results of our anvil cloud identification process are provided by region and time of day in Table 1. Altogether, anvil cloud layers are identified in 32.1% of retrieval profiles. Anvil clouds account for about one half of all cloud layers with tops above 10 km and bases above 5 km, which is consistent with previous findings that approximately half of tropical cirrus are associated with deep convection (Massie et al., 2002; Luo & Rossow, 2004). The anvil fractions found here are higher than those found by Yuan and Houze (2010), who used a TB_{11} threshold of 260 K to identify high cloud complexes, which include anvils. We find that 56.0% of the anvil profiles identified here have interpolated MODIS TB_{11} greater than 260 K, which can explain the difference between results.

Table 1. Anvil cloud identification results

	All	**Day**[a]	**Night**[b]	**West Pacific**	**Indian Ocean**
Number of profiles	4,239,774	2,119,485	2,120,641	1,808,562	2,431,212
Total Cloud Fraction	63.1%	63.4%	62.8%	71.4%	56.9%
Anvil Cloud Fraction	32.1%	33.0%	31.2%	35.0%	29.9%
Fraction of anvil cloud profiles with:					
Single anvil layer (no overlying cirrus)	84.7%	80.7%	88.8%	81.8%	87.2%
Multiple anvil layers (no overlying cirrus)	3.2%	4.0%	2.3%	3.5%	2.9%
Single anvil layer with overlying cirrus	11.9%	15.0%	8.6%	14.3%	9.7%
Multiple anvil layers with overlying cirrus	0.2%	0.4%	0.2%	0.4%	0.2%
Median properties of overlying non-anvil cirrus:					
Cloud top height (km)	15.8	15.8	15.8	16.0	15.5
Thickness (km)	0.60	0.66	0.54	0.60	0.60
Optical thickness	0.12	0.12	0.11	0.11	0.12

Note. All values are calculated from DARDAR-CLOUD after the removal of low-extinction pixels as described in section 2.2.
[a]data from 13:30 LT A-train equatorial overpass. [b]data from 01:30 LT overpass.

Table 1 provides additional information about the vertical columns in which anvil cloud layers were detected. The majority of these profiles (84.7%) contain a single anvil cloud layer that is the uppermost cloud layer in the profile. The remainder contained either multiple cloud layers meeting the anvil requirements (3.5%) or contained a non-anvil layer located above an anvil layer (12.2%), with a very small number of profiles (0.3%) falling into both categories. The presence of thin cirrus clouds above thicker anvil cirrus has been observed and discussed previously (e.g. Winker & Trepte, 1998; McFarquhar et al., 1999). Here, we find overlying cirrus layers to be more common during the day (15.4% of anvil-containing profiles) than at night (8.8%) and more common in the WP (14.7%) than in the IO (10.0%). The overlying cirrus layers identified in this analysis are optically and geometrically thin, and have a median CTH of 16.0 and 15.5 km in the WP and IO, respectively.

The values in Table 1 are calculated after the removal of low-extinction pixels to correct for the diurnal cycle of lidar sensitivity. As discussed in section 3.1, the lidar correction does not cause a significant reduction in the number of cloud layers meeting the anvil criteria. However, it does eliminate a substantial number of thin, non-anvil cirrus layers, which reduces total cloud fraction by ∼8% and the fraction of anvil clouds with an overlying cirrus layer by ∼6%. The CTH and geometric thickness of overlying non-anvil cirrus are also reduced by a few hundred meters.

4.2 Distribution of Anvil Cloud Properties

The selective cloud maintenance hypothesis argues that optically thick anvil clouds are thinned by radiative processes until they reach a more moderate optical thickness

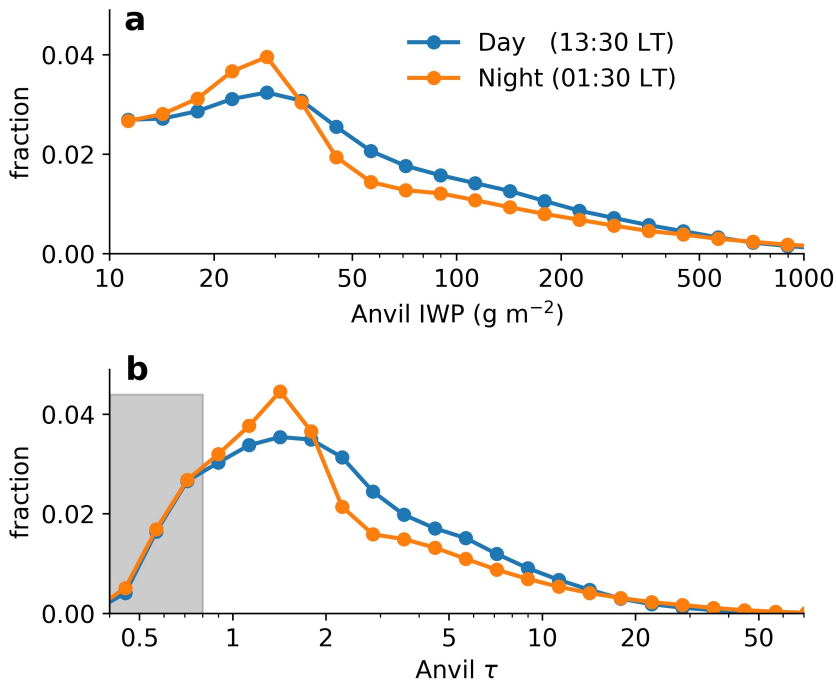

Figure 4. Anvil cloud fraction as a function of anvil (a) IWP and (b) τ at 13:30 (blue) and 01:30 (orange). In (b), the grey shading indicates the τ interval where the anvil fraction is artificially low due to the use of an IWP threshold of 10 g m^{-2} during anvil identification. Measurements are combined from the WP and IO regions. IWP and τ bin widths are 0.1 in log space.

that is then maintained by in-cloud convection. In the instantaneous snapshots provided by A-train, this would appear as a preponderance of anvil clouds with very similar τ. Figure 4 shows the observed anvil τ and IWP distributions at 13:30 and 01:30. The distributions are normalized by dividing the number of observations in each bin by the total number of retrieval profiles at 13:30 or 01:30 so that they essentially represent anvil cloud fraction as a function of IWP and τ. During both times of day, the IWP distribution peaks at $\sim$28 g m^{-2}, which matches the convective outflow peak in Figure 1 and approximately corresponds to the IWP at which high ice cloud layers exert their maximum NCRE (Berry & Mace, 2014; Hartmann & Berry, 2017). As expected, the distributions of anvil τ closely resembles those of IWP, with a peak at $\sim$1.5 at both times of day. The frequency of anvils with $\tau < 0.8$ (indicated by the grey shading in Figure 4b) is artificially reduced as a result of our requirement that anvil clouds have IWP greater than 10 g m^{-2}. The peak at $\tau \approx 1.5$, however, is not an artifact. Anvil clouds with τ between 1 and 2 typically have IWP that 2-3 times higher than the threshold (Figure S2), and the τ distribution for $\tau > 0.8$ is unaffected if the threshold is reduced (Figure S3). Further discussion of this issue is provided in section S1. We examined the influence of retrieval error on the τ distribution using the pixel-by-pixel α_v error values provided in DARDAR-CLOUD. Anvil τ was recalculated for the low- and high-α_v cases. The modal τ varies between $\sim$1.1 and $\sim$2.2 in the low- and high-α_v cases, respectively, but the distribution always retains its same basic shape.

There are two important differences between the 13:30 and 01:30 anvil IWP distributions. First, the 01:30 distribution contains fewer clouds with IWP greater than 40 g m^{-2} ($\tau \gtrsim 2$). Can this be explained by the daily cycle of deep convection and the timing of the A-train equatorial crossings? Convective activity in maritime regions is high-

est between 05:00 and 07:00 LT and is lowest during the evening hours, though the magnitude of the daily cycle is weak and MCSs are observed readily throughout the day (Nesbitt & Zipser, 2003). The 13:30 overpass takes place about 7 hours after the peak in convective activity and would therefore encounter a"fresher" anvil cloud population that the 01:30 overpass, which occurs 19 hours after the peak. This is consistent with the reduced presence of high-IWP clouds at 01:30, if it can be assumed that a cloud population tends towards lower IWP as it ages. This brings us to the second important difference in the distributions: anvils with an IWP of 20-35 g m^{-2} ($1 \lesssim \tau \lesssim 2$) are more frequent at 01:30, but those with an even lower IWP of 10-20 g m^{-2} ($\tau \lesssim 1$) are found at a similar frequency at both times of day. As a result, the distribution peak is more pronounced at 01:30 than at 13:30. This change in the shape of the distribution is consistent with the maintenance of clouds with τ between 1 and 2: as time progresses, anvil clouds progress towards this τ range but do not continue to thin as rapidly after that.

To confirm that anvil clouds with $1 < \tau < 2$ (which we refer to as "modal anvils" from now on) are indeed older than optically thicker ones, we examine the distribution of anvil d_{core} and how τ varies with spreading distance. A histogram of d_{core} using a bin width of 5 km is shown in Figure 5a. The high number of anvil profiles in the lowest d_{core} bin reflects the misclassification of optically thick anvils with TB_{11} below 210 K as convective cores. Other than this, the distribution shows a broad peak between 30 and 60 km, beyond which frequency decays exponentially. Approximately one third of anvil profiles are located further than 250 km from the nearest core. The evolution of τ with spreading distance can be seen in Figure 5b, which shows a joint histogram of τ and d_{core} normalized so that the sum of frequencies in each d_{core} bin is equal to one. The black line indicates median τ for the observations in each d_{core} bin. Anvils are typically detrained with τ greater than 10. Median τ decreases exponentially with distance until ∼40 km, at which point it decreases slowly as it nears the modal range of 1-2. The τ distribution does not change much beyond 300 km (it is only shown up to 500 km in Figure 5b), suggesting that anvil clouds located far from their convective source tend to assume a common form.

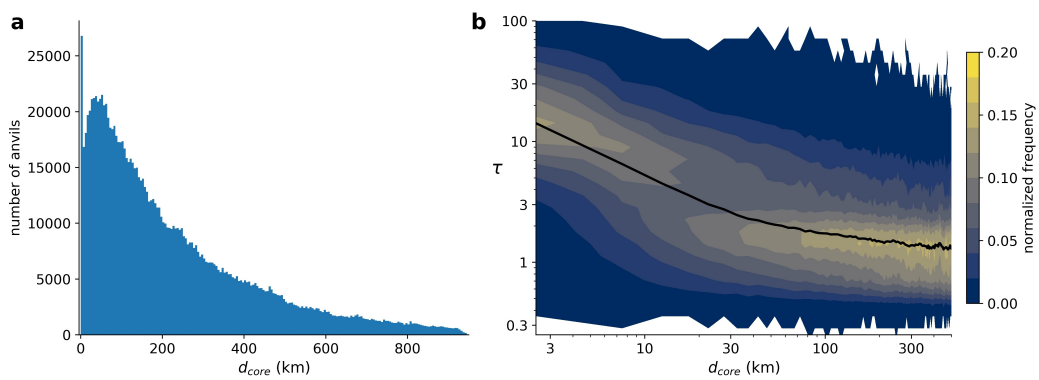

Figure 5. (a) Histogram of anvil cloud spreading distance, d_{core}. (b) Joint histogram of anvil d_{core} and τ, with frequency normalized by column so that the values in each d_{core} bin add up to one. The black line indicates the median τ for each d_{core} bin. The d_{core} bin width is 5 km in both plots. Note the differences between the x-axes of (a) and (b) and the logarithmic scale of both axes in (b).

So far, we have shown a preponderance of anvil clouds with τ between 1 and 2 at both 13:30 and 01:30 and that these modal anvils can readily be observed several hundred kilometers away from the nearest convective core. Together, these two findings offer support for the hypothesis that anvils are driven towards and maintained at an op-

tical thickness corresponding to a positive NCRE. They do not, however, provide insight into the mechanisms responsible for cloud maintenance. To examine this question, we must assess how cloud geometries and radiative heating profiles evolve with optical thinning.

4.3 Macrophysical Structure and Radiative Heating

Changes in cloud properties such as geometric thickness and CTH can provide further insight into the processes responsible for anvil cloud maintenance. The evolution of these properties with respect to τ at different times of day and in the different study regions is shown in Figure 6. The contour plots show vertically resolved anvil cloud fraction and median CTH and CBH; here, the cloud fraction at a specific altitude and τ can be interpreted as the probability of finding anvil cloud at that altitude provided that there is an anvil cloud with optical depth τ somewhere in the vertical column. These composites thus reflect the typical height and vertical extent of anvils at different stages of optical thinning. Median geometric thickness is shown below the corresponding cloud fraction composites (shading is between the 25th and 75th percentiles). The corresponding radiative heating calculations are shown in Figure 7, along with the vertically mass-averaged net heating ($\overline{Q}_R$) and radiative lapse rate tendency (LRT). Anvil cloud evolution and its diurnal differences are more pronounced in the WP than in the IO but are qualitatively similar in both regions; for the sake of simplicity, any numeric values referenced in our discussion are for the WP.

The properties of freshly detrained anvils can be seen at $\tau \gtrsim 10$ in Figures 6 and 7. The median CTH of the optically thickest anvils is similar between day and night, which suggests that anvil tops are detrained at a relatively constant altitude throughout the day. Geometric thickness is typically between 6 and 9 km and is slightly greater during the day due to the lower CBH found then. Lilly (1988) described how a fresh convective outflow plume is flattened by negative buoyancy at cloud top and positive buoyancy at cloud base. Our calculations suggest that this buoyancy is strengthened at night by strong radiative cooling at cloud top and heating at cloud base on the order of -20 and 14 W m^{-2}, respectively. Because there is both heating and cooling, $\overline{Q}_R$ is small at night. During the day, $\overline{Q}_R$ is elevated to $\sim$3 W m^{-2} due to the addition of SW heating, which nearly cancels out the LW cooling at cloud top and counteracts the negative buoyancy there.

Could the diurnal difference in the radiative heating of freshly detrained anvil clouds influence their evolution? To answer this, we inspect how the properties of moderately thick clouds ($4 < \tau < 10$) differ between day and night. At 01:30, the typical CTH of moderately thick anvils is about 1 km lower than that of optically thick anvils; this drop is consistent with the initial negative buoyancy at cloud top and its hastening by LW cooling. At 13:30, the CTH of moderately thick anvils is similar to that of optically thicker ones, suggesting that cloud top does not sink as rapidly then, perhaps due to the cancellation of LW cooling by SW heating. As a result of this CTH maintenance, anvils with $\tau > 4$ are geometrically thicker at 13:30 than they are at 01:30. It thus seems possible that radiative heating plays a significant role in the initial evolution of freshly detrained anvils by hastening their geometric thinning at night and hindering it during the day.

As τ decreases from 10 to 4, the net heating of anvil clouds increases. Continued rise in CBH causes the temperature difference between cloud base and the surface to increase, which results in a moderate strengthening of LW heating. As the heated region moves upwards, LW cooling at cloud top weakens and is eventually overcome by solar heating during the day, at which point the layer is heated throughout. Geometric thinning over this τ interval is greater at 13:30 than at 01:30 due to a greater rise in CBH. By $\tau \approx 4$, thickness is similar at both times of day, but $\overline{Q}_R$ is almost twice as strong at 13:30 than at 01:30.

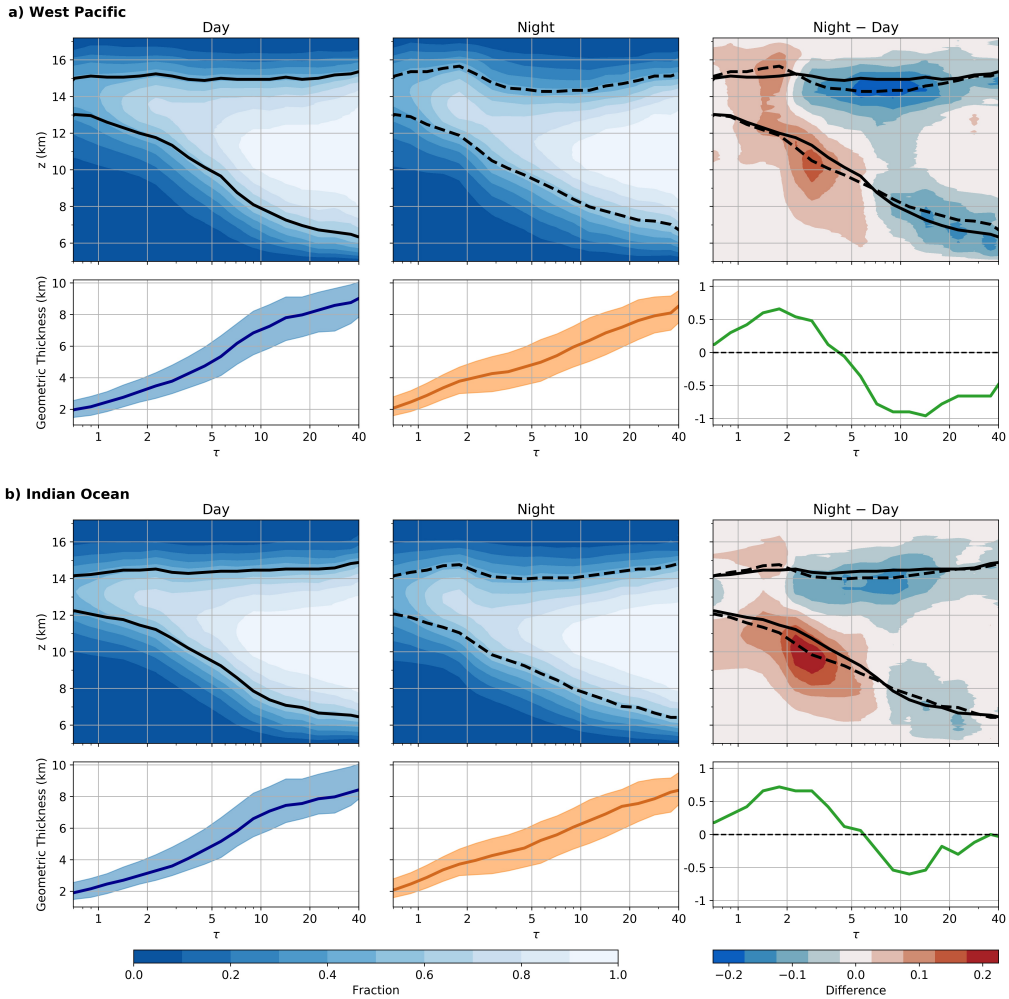

Figure 6. Anvil cloud geometry as a function of τ in the (a) West Pacific and (b) Indian Ocean regions, shown for (left) day, (middle) night, and (right) night minus day. For each region and time of day, the top plot shows the fraction of anvil clouds profiles in each τ bin that contain cloud at a given altitude. Black lines (solid for day, dashed for night) show the median CTH and CBH for each τ bin. The bottom plot shows median geometric thickness, with shading indicating the 25th to 75th percentiles. The green line shows the difference in median geometric thickness between night and day.

Several interesting shifts occur as τ approaches the modal range of 1-2. At night, LW cooling at cloud top ceases, and median CTH simultaneously rises by 1.2 km to its highest value (15.7 km) at $\tau \approx 1.8$. Because CTH rises nearly as quickly as CBH, there is little geometric thinning as τ decreases from 4 to 2. During the day, cloud property changes over this τ interval are quite different. The rise in CTH is more modest (only ∼300 m), but CBH rise is similar, which results in greater geometric thinning during the day than at night. In the modal τ range, daytime anvils are ∼600 m thicker and have a median CTH that is ∼500 m higher than nighttime anvils.

The geometric differences between modal anvils observed during day and night have important implications for the mass-averaged heating $\overline{Q}_R$ (purple lines in Figure 7), which

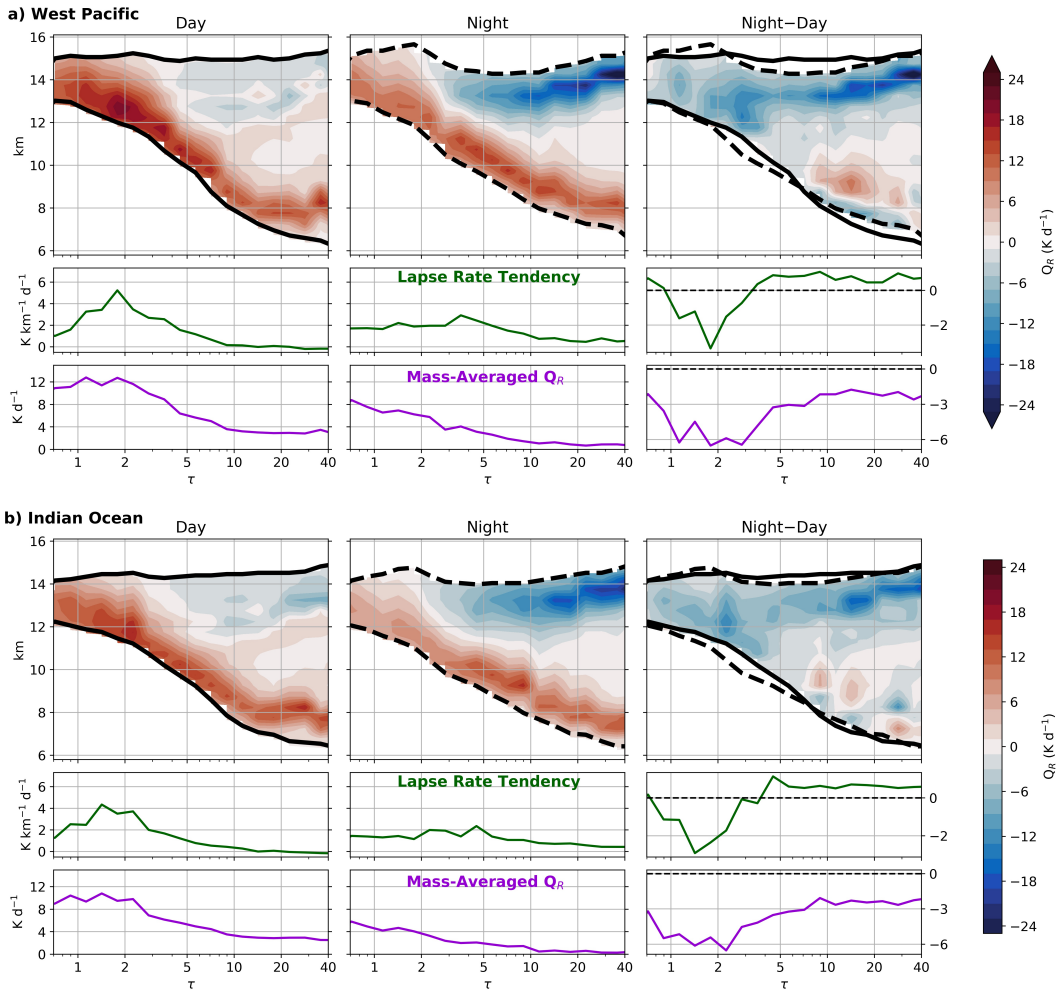

Figure 7. Modeled anvil cloud radiative heating for typical anvil geometries in the (a) West Pacific and (b) Indian Ocean regions for (left) day, (middle) night, and (right) night minus day. For each region, the top row of plots shows net radiative heating (equal to the sum of SW and LW heating during the day and just equal to LW heating at night), and the black lines (solid for day, dashed for night) show the median CTH and CBH for each τ bin. The middle row gives the mass-averaged lapse rate tendency as calculated from corresponding heating rates, and the bottom row gives the mass-averaged layer heating ($\overline{Q}_R$).

is generally higher in the modal τ range than it is at larger τ. Because daytime anvils are geometrically thinner than nighttime anvils of equal τ, they must have a higher in-cloud α_v on average. The higher α_v results in greater LW flux convergence near cloud base and thus stronger radiative heating there. Because of this geometric effect, the mass-averaged LW heating of anvils with $\tau \approx 1.8$ is greater during the day (8.2 W m^{-2}) than at night (6.2 W m^{-2}). The addition of solar heating during the day results in a net $\overline{Q}_R$ of 12.7 W m^{-2}, more than twice the nighttime value.

The geometry of modal anvils also affects their susceptibility to radiative destabilization, as indicated by the LRT (green lines in Figure 7). The decrease in LW heating with altitude destabilizes the vertical column and generates a positive LRT. The geometric effect described in the previous paragraph causes not only stronger LW heat-

ing in modal anvils at 13:30, but also stronger heating gradients. Modal anvils observed at 13:30 consequently experience a higher LRT than those at 01:30. Solar heating during the day is strongest near cloud top and therefore acts to decrease LRT, but does not provide enough stabilization to overcome the geometric effect. As a result, LRT in the modal τ range is about twice as high at 13:30 than it is at 01:30. During the day, the maximum LRT occurs in the modal τ range. At night, LRT varies much less for $\tau \lesssim 5$ but has a slight maximum at $\tau \approx 4$, when the layer is still optically thick enough to have a LW heating dipole that strengthens the vertical heating gradient. Still, the maximum nighttime LRT is only about half of the maximum daytime LRT.

It may seem contradictory that modal anvils are typically found at lower altitudes at 13:30 than at 01:30 despite the fact that those 13:30 are heated and destabilized more strongly and should therefore gain more buoyancy. This is reconciled by the fact that detrained cirrus can persist for much longer than the 12 hours between the two A-train equatorial crossings (Luo & Rossow, 2004). It is possible that most of the modal anvils observed at 01:30 were detrained during the day, when solar heating would have initially maintained their CTH and slowed their geometric thinning. As they evolve, they could retain higher CTH and thicker geometry relative to anvils detrained at night (but observed at 13:30), which would experience CTH subsidence and faster geometric thinning. This explanation suggests that the life cycle of convective outflow is subject to hysteresis, in which the initial evolution of a freshly detrained cloud influences its properties later on. It could then be the case that the nighttime increase in anvil CTH as τ approaches the modal range represents a shift in the anvil cloud population from those that were detrained at night to those detrained during the day.

It is also possible that the thinner geometry of daytime modal anvils is the product of natural selection. If destabilization is critical to anvil maintenance, then the stabilizing effect of solar heating would impede the persistence of anvils during the day. We have already discussed how thinner geometry compensates for solar stabilization by promoting stronger gradients in LW heating. It follows that geometrically thinner anvils are better suited to withstand solar stabilization than thicker ones and would therefore be more likely to persist and be observed during the day. At night, in the absence of solar heating, such a thin geometry would not be required for cloud maintenance. It may be that the the diurnal difference in anvil structure results partly from this selection and partly from the hysteresis described in the previous paragraph.

In this section, we have shown that radiative heating hastens anvil thinning at night but hinders it during the day, and we suggest that this has an impact on anvil properties down the line. As anvil clouds evolve, they are increasingly heated and destabilized by LW radiation. Radiative destabilization is strongest in clouds with modal τ observed during the day, which are geometrically thinner than those observed at night. In general, modal anvils undergo stronger mass-averaged heating than their optically thick precursors and are located at higher altitudes. The especially high altitude of modal anvils observed at 01:30 may result from their initial detrainment during the day, when solar heating counteracts negative buoyancy at cloud top. The findings of this section underscore the importance of radiative heating in anvil clouds evolution and are consistent with the selective maintenance hypothesis. The radiative destabilization of modal anvils offers support for the microphysical cycling mechanism, which is explored further in the next section.

4.4 Microphysical Structure

In-cloud convection plays an important role in the microphysical cycling mechanism of anvil cloud maintenance proposed by Hartmann et al. (2018), in which a cycle of freezing and sublimation in turbulent eddies counteracts sedimentation and preserves cloud ice content. To evaluate this mechanism, we turn to DARDAR retrievals of anvil

microphysical structure. Composites of r_e, N_i, and IWC are shown in Figure 8 and 9 for the WP and IO regions, respectively. These composites are generated in the same way as those used in the radiative heating calculations (see section 3.4) and thus correspond to the heating rates shown in Figure 7. This representation allows us to inspect anvil microphysical structure and its evolution with optical thinning.

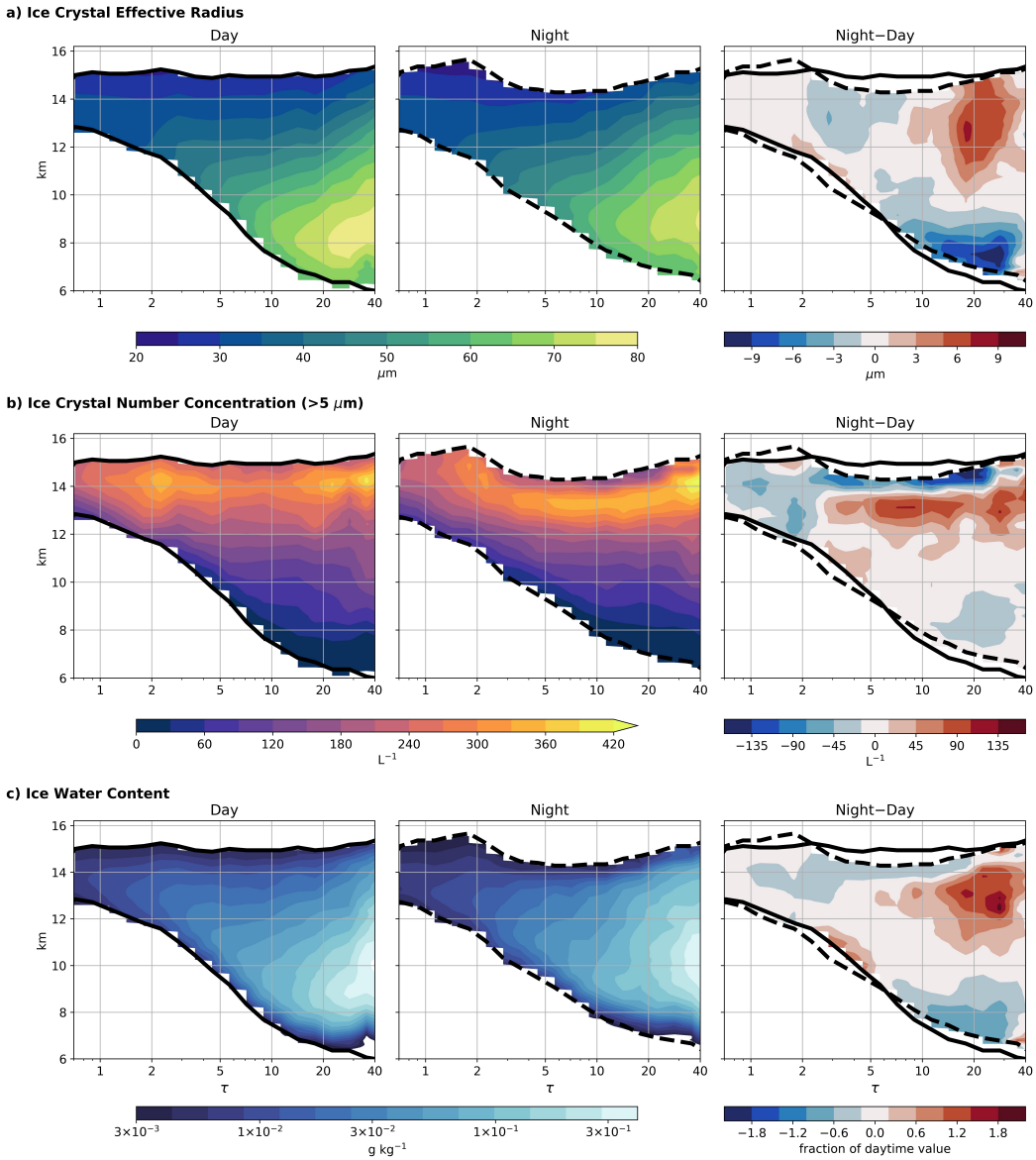

Figure 8. Composites of median (a) effective radius, r_e, (b) number concentration of ice crystals with a maximum diameter exceeding 5 μm, N_i, and (c) ice water content, IWC, for anvil clouds in the West Pacific for (left) day, (middle) night, and (right) night minus day. Black lines (solid for day, dashed for night) indicate median cloud top and base heights. In (c), the color shading for the day and night composites uses a logarithmic scale, and the night minus day difference is expressed as a fraction of the daytime value.

The anvil cloud vertical structure found here is consistent with in situ aircraft measurements (McFarquhar & Heymsfield, 1996; Heymsfield et al., 2002; Jensen et al., 2009;

Lawson et al., 2010) and with satellite observations of radar reflectivity within anvil clouds connected to active MCSs (Yuan et al., 2011). Median r_e generally decreases with altitude, as expected from gravitational size sorting and the temperature dependence of ice diffusional growth. N_i, which is dominated by smaller ice crystals, generally increases with height until its maximum ∼1 km below cloud top. Despite high N_i near cloud top, maximum IWC is typically found 1-2 km above cloud base and decreases with altitude above that point, suggesting that total IWC is dominated by large ice crystals. The layer of low IWC at cloud base, sometimes accompanied by smaller r_e, likely reflects a subsaturated layer where ice crystal sublimation occurs. The vertical structure of α_v (not shown) is very similar to that of IWC; this is consistent with the finding that the radiative properties of anvil clouds are dominated by large ice crystals (Jensen et al., 2009; Lawson et al., 2010).

Diurnal variations in anvil vertical structure are evident in optically thick clouds ($\tau \gtrsim 10$), which are freshly detrained and generally located close to a convective core (see Figure 5). In both study regions, these clouds are more "top-heavy" at night, in that median r_e, IWC, and N_i are larger in the upper half of the cloud and smaller in the bottom half than they are during the day. Since top-heaviness would be expected to generally decrease with time as large ice crystals settle, it could be the case that optically thick anvils observed at 01:30 were detrained more recently than those observed at 13:30. However, this seems unlikely for the same reasons why we believe the convective cloud population observed at 01:30 is more aged than that at 13:30 (see section 4.2). Can the diurnal differences in vertical structure be explained by differences in convective intensity? If deep convective updrafts were stronger at night, larger ice crystals would be carried higher into the atmosphere, and freshly detrained anvils would appear more top heavy. Nesbitt and Zipser (2003) found that the diurnal cycle of convective precipitation over tropical oceans is driven almost entirely by the number of MCSs rather than their intensity, which varies only minimally throughout the day. It thus seems unlikely that convective intensity is responsible for the diurnal variation in the vertical structure of freshly detrained anvils. The causes of the top-heavy structure observed at 01:30 are worthy of further study.

While anvil vertical structure is qualitatively consistent across the entire τ range considered here, its quantitative evolution with respect to τ is less straightforward. As τ decreases from 40 to ∼10, the median IWC and r_e at a fixed altitude fall substantially, as evidenced by the positively sloped IWC and r_e contours at high τ in Figures 8 and 9. Cloud-top N_i also falls, but the decrease is not monotonic in every composite. This factor-of-four decrease in τ is accompanied by only a 22% decrease in geometric thickness, suggesting that optical thinning occurs on faster timescales than geometric thinning during the initial stages of evolution. This could reflect anvil precipitation, and is consistent with simulations showing the relatively rapid fallout of large ice crystals after detrainment (Jensen et al., 2018). This pattern reverses around $\tau \approx 10$, when geometric thickness begins to rapidly decrease and the IWC and r_e contours flatten. This transition is more apparent in the 13:30 composites than in the 01:30 composites and is indicative of a microphysical equilibrium in which r_e and IWC remain relatively constant at a fixed altitude level. A similar equilibrium was noted by Gallagher et al. (2012) during aircraft sampling of convective outflow and was attributed to a balance between the growth of ice crystals by aggregation and their removal by sedimentation.

The evolution of cloud-top N_i with decreasing τ is perhaps our most interesting finding. Number concentrations are highest in freshly detrained anvils and initially decrease with optical thinning. Over the course of this thinning, N_i is nearly always higher at the time when the clouds are more susceptible to radiative destabilization (i.e., when they are geometrically thinner and have a higher LRT). This means that N_i is higher at night for $\tau \gtrsim 4$ and during the day for $\tau \lesssim 4$. There is a relative N_i minimum at some τ between 3 and 7, depending on the region and time. As τ approaches its modal

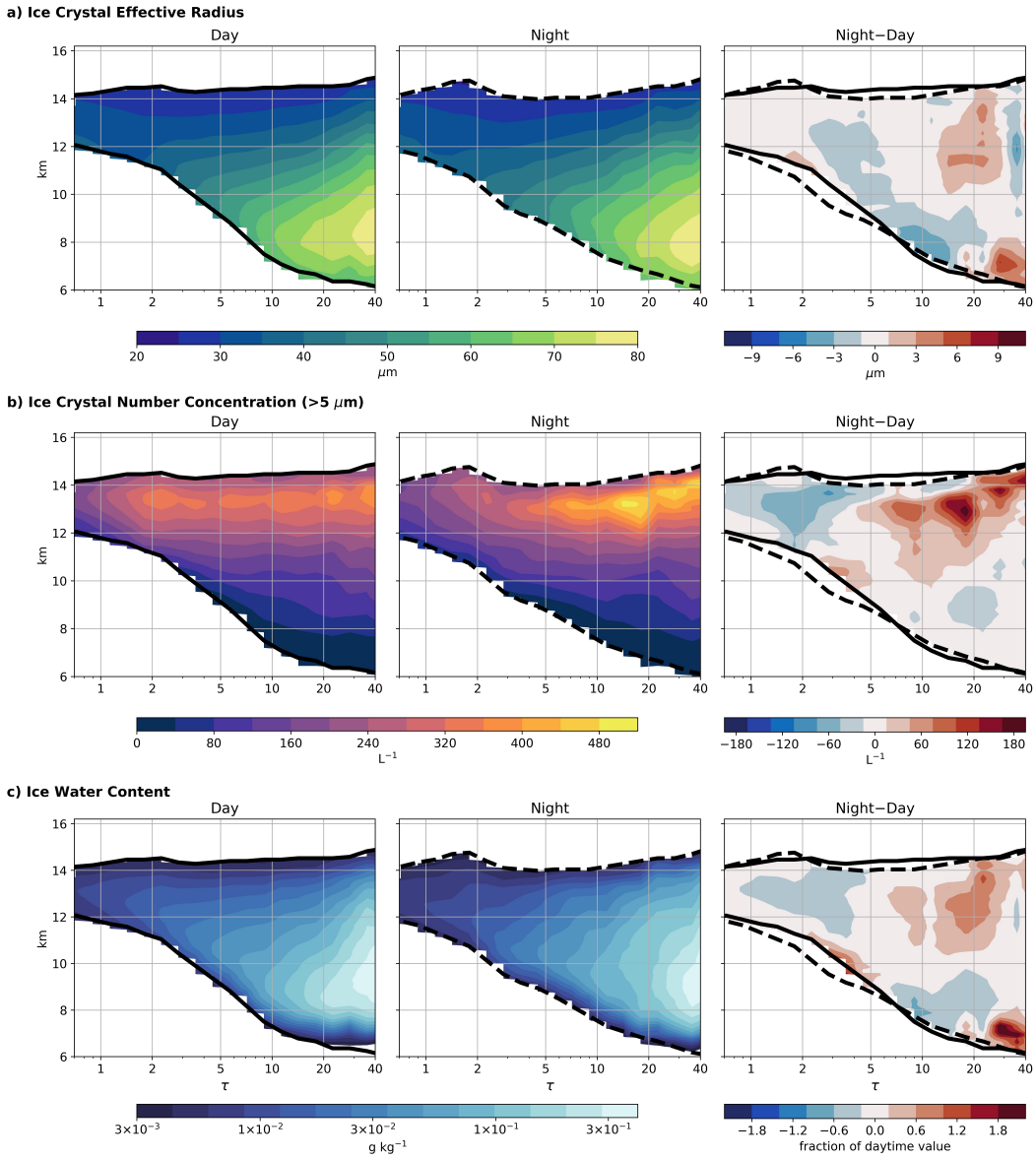

Figure 9. As in Figure 8, but for the Indian Ocean region.

range, there is a resurgence in N_i that is present in all of the composites but is much more pronounced during the day, when the resurgence peaks at $\tau \approx 2.2$. This coincides exactly with a large daytime increase in radiative LRT and $\overline{Q}_R$ in the IO region (see Figure 7). In the WP region, LRT is also increasing at this point, but its largest spike is found in the next lowest τ bin ($\tau \approx 1.8$). At night, when there is no notable increase in LRT at the modal τ but rather a rise in CTH, the N_i resurgence at $\tau \approx 2.2$ is much less pronounced, constituting only a minor disruption to the general decrease in cloud-top N_i that accompanies optical thinning. Since the DARDAR-NICE retrieval relies partly on empirical parameterizations involving temperature, it is possible that the temperature decrease accompanying the rise in altitude at this point plays a role in the N_i resurgence.

The association of high LRT with elevated N_i suggests that radiatively driven turbulence preserves ice crystal number and is consistent with the microphysical cycling mechanism proposed Hartmann et al. (2018). Turbulence can maintain N_i by driving new ice

crystal nucleation, counteracting sedimentation, or some combination thereof. The higher number concentrations found at the modal τ compared to those at slightly higher τ suggests that at least some fresh nucleation occurs. It is possible that the N_i resurgence is somewhat exaggerated in Figures 8 and 9 due to effect of initial detrainment time discussed in the previous section. The daytime N_i increase at $\tau \approx 2.2$ could coincide with a shift in the anvil cloud population towards those that were originally detrained at night, when ice concentrations in freshly detrained anvils are typically higher than they are during the day. Even if this were the case, the high N_i in modal anvils would still reflect the preservation of ice crystal number against sedimentation over large distances and timescales.

The composites of anvil microphysical structure shown in Figures 8 and 9 reflect the median microphysical quantities of anvil cloud profiles meeting the CTH and CBH requirements described in section 3.4. To test the sensitivity of our results to this methodology, we uniformly adjusted the CTH range used to select qualifying profiles for each τ bin. This has the effect of shifting the entire anvil composite to a different altitude while maintaining the relative altitude differences between different τ. We made adjustments in 1-km increments ranging from a 3-km decrease in altitude to a 1-km increase and found that a cloud-top N_i resurgence is always present somewhere between optical depths 1.8 and 3. In fact, the N_i resurgence is sometimes even more pronounced at different altitude levels than it is at the median altitude range. While the microphysical evolution depicted in Figures 8 and 9 is qualitatively robust, we note that there is substantial variability in microphysical quantities within each τ-altitude bin; we have chosen to show median values here to minimize the influence of outliers and convey the typical structure of anvil clouds of different τ. Results are qualitatively similar if mean quantities are used instead. It is also important to note that there is substantial uncertainty associated with the microphysical retrievals in DARDAR-CLOUD and DARDAR-NICE (for discussion, see Delanoë & Hogan, 2010; Sourdeval et al., 2018). The consistency of the anvil vertical structure found here with in situ observations provides confidence in the microphysics retrievals and the robustness of our results.

5 Summary and Conclusions

We have provided a large-scale assessment of the macrophysical and microphysical evolution of tropical anvil clouds. Clouds associated with deep convection impart a distinct signature on the climatological distribution of cloud layer IWP that allows them to be distinguished from the thin cirrus clouds that blanket the tropical tropopause layer. The evolution of convective outflow from freshly detrained, optically thick anvil clouds to thin cirrus with a positive NCRE is evident in the satellite record but requires both a radar and a lidar to detect, as has been noted previously (Berry & Mace, 2014). Our use of a combined radar-lidar retrieval has allowed us to carefully select cloud layers that are likely of convective origin and to assess previously proposed mechanisms of anvil maintenance.

The satellite observations examined here provide support for the selective cloud maintenance hypothesis proposed by Hartmann and Berry (2017), which states that anvil clouds are driven towards an optical thickness that allows for their maintenance over time by radiative heating. We find that anvil clouds with an optical depth between 1 and 2 ("modal" anvils) are prevalent in tropical convective regions and can persist hundreds of kilometers away from a detectable convective source. In general, modal anvils experience stronger mass-averaged radiative heating and greater radiative destabilization than optically thicker clouds and are typically located at higher altitudes, especially during the 01:30 A-train equatorial overpass. They are also found to have higher ice number concentrations at cloud top, which suggests that new ice crystal nucleation and/or the suppression of sedimentation play a role in cloud maintenance. Elevated number concentrations are most apparent during the day, when the geometric and optical characteristics of modal anvils render them particularly prone to vertical destabilization by LW radiative heating. At

night, when modal anvils are geometrically thicker and less susceptible to radiative destabilization, the number concentration resurgence is correspondingly weaker. The association of high number concentration with stronger radiative destabilization lends support for the microphysical cycling mechanism of anvil cloud maintenance proposed by Hartmann et al. (2018).

Despite stronger radiative heating and destabilization, modal anvils observed at 13:30 are located at lower altitudes than those observed at 01:30; to explain this apparent discrepancy, we hypothesize that the properties of aged anvil clouds are determined in part by the time of day at which they first detrained. It is likely that many modal anvils observed at 13:30 were detrained during the preceding night, when strong LW cooling promotes cloud-top subsidence and hastens the geometric thinning of freshly detrained anvils. On the other hand, modal anvils detected at 01:30 could have been detrained during the day, when SW heating hinders cloud top subsidence and geometric thinning. This suggests that the initial time of detrainment has influence over the altitude and thickness of an anvil cloud throughout its life cycle, which in turn determine a cloud's susceptibility to different maintenance processes. The rapid geometric thinning of anvil clouds detrained at night facilitates stronger radiative heating and destabilization later on. Meanwhile, the slower thinning of anvil clouds detrained during the day allows their tops to persist at higher altitudes but results in weaker heating. Hysteresis could have important implications for anvil cloud evolution in a changing climate and is worthy of further study using cloud-resolving models that include a realistic diurnal cycle of insolation.

The present study underscores the importance of radiative, turbulent and microphysical processes in determining the NCRE in tropical convective regions. Future work should focus on how the cloud maintenance processes examined here interact with other changes that are expected to result from greenhouse gas warming. In a warmer world, tropical convection is expected to be more aggregated (Emanuel et al., 2014), and anvil clouds are expected to move upwards in altitude (Hartmann & Larson, 2002), where they may encounter an increasingly stable environment (Zelinka & Hartmann, 2010). The impact of these changes on high cloud fraction remains uncertain, with some models predicting varying degrees of reduction (Tompkins & Craig, 1999; Bony et al., 2016; Li et al., 2019) and others predicting an increase (Ohno et al., 2019). Discussions of future anvil cloud amount have typically focused on changes in the amount of convective detrainment; our results show that post-detrainment maintenance processes must also be considered.

Acknowledgments

Support for this research was provided by the National Science Foundation under grant AGS-1549579. We thank Bla Gasparini for insightful discussions that improved this work. DARDAR data was obtained from the ICARE Data and Services Center (http://www.icare.univ-lille1.fr/projects/dardar) and MODIS data from the NASA Level-1 and Atmosphere Archive and Distribution System (https://ladsweb.modaps.eosdis.nasa.gov). The derived data and radiative heating model results needed to reproduce the figures in this paper are available at http://hdl.handle.net/1773/45556.

References

Ackerman, T. P., Liou, K. N., Valero, F. P., & Pfister, L. (1988). Heating rates in tropical anvils. *Journal of the Atmospheric Sciences*, *45*(10), 1606–1623. doi: 10.1175/1520-0469(1988)045⟨1606:HRITA⟩2.0.CO;2

Berry, E., & Mace, G. G. (2014, 8). Cloud properties and radiative effects of the Asian summer monsoon derived from A-Train data. *Journal of Geophysical Re-*

search, *119*(15), 9492–9508. doi: 10.1002/2014JD021458

Bony, S., Stevens, B., Coppin, D., Becker, T., Reed, K. A., Voigt, A., & Medeiros, B. (2016). Thermodynamic control of anvil cloud amount. *Proceedings of the National Academy of Sciences of the United States of America*. doi: 10.1073/pnas.1601472113

Bretherton, C. S., Blossey, P. N., & Khairoutdinov, M. (2005). An energy-balance analysis of deep convective self-aggregation above uniform SST. *Journal of the Atmospheric Sciences*. doi: 10.1175/JAS3614.1

Cazenave, Q., Ceccaldi, M., Delanoë, J., Pelon, J., Groß, S., & Heymsfield, A. (2019, 5). Evolution of DARDAR-CLOUD ice cloud retrievals: New parameters and impacts on the retrieved microphysical properties. *Atmospheric Measurement Techniques*, *12*(5), 2819–2835. doi: 10.5194/amt-12-2819-2019

Delanoë, J., & Hogan, R. J. (2008, 4). A variational scheme for retrieving ice cloud properties from combined radar, lidar, and infrared radiometer. *Journal of Geophysical Research Atmospheres*, *113*(7). doi: 10.1029/2007JD009000

Delanoë, J., & Hogan, R. J. (2010). Combined CloudSat-CALIPSO-MODIS retrievals of the properties of ice clouds. *Journal of Geophysical Research Atmospheres*, *115*(4). doi: 10.1029/2009JD012346

Delanoë, J., Protat, A., Jourdan, O., Pelon, J., Papazzoni, M., Dupuy, R., ... Jouan, C. (2013, 1). Comparison of Airborne In Situ, Airborne RadarLidar, and Spaceborne RadarLidar Retrievals of Polar Ice Cloud Properties Sampled during the POLARCAT Campaign. *Journal of Atmospheric and Oceanic Technology*, *30*(1), 57–73. doi: 10.1175/JTECH-D-11-00200.1

Deng, M., Mace, G. G., Wang, Z., & Paul Lawson, R. (2013). Evaluation of several A-Train ice cloud retrieval products with in situ measurements collected during the SPARTICUS campaign. *Journal of Applied Meteorology and Climatology*. doi: 10.1175/JAMC-D-12-054.1

Dobbie, S., & Jonas, P. (2001, 10). Radiative influences on the structure and lifetime of cirrus clouds. *Quarterly Journal of the Royal Meteorological Society*, *127*(578), 2663–2682. doi: 10.1002/qj.49712757808

Emanuel, K., Wing, A. A., & Vincent, E. M. (2014). Radiative-convective instability. *Journal of Advances in Modeling Earth Systems*. doi: 10.1002/2013MS000270

Fu, Q., Yang, P., & Sun, W. B. (1998, 9). An Accurate Parameterization of the Infrared Radiative Properties of Cirrus Clouds for Climate Models. *Journal of Climate*, *11*(9), 2223–2237. doi: 10.1175/1520-0442(1998)011⟨2223:AAPOTI⟩2.0.CO;2

Gallagher, M. W., Connolly, P. J., Crawford, I., Heymsfield, A., Bower, K. N., Choularton, T. W., ... Hacker, J. (2012, 7). Observations and modelling of microphysical variability, aggregation and sedimentation in tropical anvil cirrus outflow regions. *Atmospheric Chemistry and Physics*, *12*(14), 6609–6628. doi: 10.5194/acp-12-6609-2012

Gasparini, B., Blossey, P. N., Hartmann, D. L., Lin, G., & Fan, J. (2019, 7). What drives the lifecycle of tropical anvil clouds? *Journal of Advances in Modeling Earth Systems*, 2019MS001736. doi: 10.1029/2019MS001736

Gettelman, A., Salby, M. L., & Sassi, F. (2002, 5). Distribution and influence of convection in the tropical tropopause region. *Journal of Geophysical Research D: Atmospheres*, *107*(9-10), 6–1. doi: 10.1029/2001jd001048

Harrison, E. F., Minnis, P., Barkstrom, B. R., Ramanathan, V., Cess, R. D., & Gibson, G. G. (1990). Seasonal variation of cloud radiative forcing derived from the Earth Radiation Budget Experiment. *Journal of Geophysical Research*, *95*(D11). doi: 10.1029/jd095id11p18687

Hartmann, D. L. (2016). *Tropical anvil clouds and climate sensitivity.* doi: 10.1073/pnas.1610455113

Hartmann, D. L., & Berry, S. E. (2017). The balanced radiative effect of tropical

anvil clouds. *Journal of Geophysical Research*, *122*(9), 5003–5020. doi: 10.1002/2017JD026460

Hartmann, D. L., Gasparini, B., Berry, S. E., & Blossey, P. N. (2018, 12). The Life Cycle and Net Radiative Effect of Tropical Anvil Clouds. *Journal of Advances in Modeling Earth Systems*, *10*(12), 3012–3029. doi: 10.1029/2018MS001484

Hartmann, D. L., & Larson, K. (2002). An important constraint on tropical cloud - climate feedback. *Geophysical Research Letters*. doi: 10.1029/2002gl015835

Hartmann, D. L., Moy, L. A., & Fu, Q. (2001). Tropical convection and the energy balance at the top of the atmosphere. *Journal of Climate*. doi: 10.1175/1520-0442(2001)014⟨4495:TCATEB⟩2.0.CO;2

Heymsfield, A. J., Bansemer, A., Field, P. R., Durden, S. L., Stith, J. L., Dye, J. E., . . . Grainger, C. A. (2002). Observations and parameterizations of particle size distributions in deep tropical cirrus and stratiform precipitating clouds: Results from in situ observations in TRMM field campaigns. *Journal of the Atmospheric Sciences*, *59*(24), 3457–3491. doi: 10.1175/1520-0469(2002)059⟨3457:OAPOPS⟩2.0.CO;2

Iacono, M. J., Mlawer, E. J., Clough, S. A., & Morcrette, J.-J. (2000, 6). Impact of an improved longwave radiation model, RRTM, on the energy budget and thermodynamic properties of the NCAR community climate model, CCM3. *Journal of Geophysical Research: Atmospheres*, *105*(D11), 14873–14890. doi: 10.1029/2000JD900091

Igel, M. R., Drager, A. J., & van den Heever, S. C. (2014, 9). A CloudSat cloud object partitioning technique and assessment and integration of deep convective anvil sensitivities to sea surface temperature. *Journal of Geophysical Research: Atmospheres*, *119*(17), 10515–10535. doi: 10.1002/2014JD021717

Jensen, E. J., Lawson, P., Baker, B., Pilson, B., Mo, Q., Heymsfield, A. J., . . . Tanelli, S. (2009). On the importance of small ice crystals in tropical anvil cirrus. *Atmospheric Chemistry and Physics*. doi: 10.5194/acp-9-5519-2009

Jensen, E. J., van den Heever, S. C., & Grant, L. D. (2018, 9). The Life Cycles of Ice Crystals Detrained From the Tops of Deep Convection. *Journal of Geophysical Research: Atmospheres*, *123*(17), 9624–9634. doi: 10.1029/2018JD028832

Lawson, R. P., Jensen, E., Mitchell, D. L., Baker, B., Mo, Q., & Pilson, B. (2010). Microphysical and radiative properties of tropical clouds investigated in TC4 and NAMMA. *Journal of Geophysical Research*. doi: 10.1029/2009jd013017

Li, R. L., Storelvmo, T., Fedorov, A. V., & Choi, Y.-S. (2019, 8). A Positive Iris Feedback: Insights from Climate Simulations with Temperature-Sensitive CloudRain Conversion. *Journal of Climate*, *32*(16), 5305–5324. doi: 10.1175/JCLI-D-18-0845.1

Lilly, D. K. (1988). Cirrus outflow dynamics. *Journal of the Atmospheric Sciences*, *45*(10), 1594–1605. doi: 10.1175/1520-0469(1988)045⟨1594:COD⟩2.0.CO;2

Luo, Z., & Rossow, W. B. (2004, 12). Characterizing Tropical Cirrus Life Cycle, Evolution, and Interaction with Upper-Tropospheric Water Vapor Using Lagrangian Trajectory Analysis of Satellite Observations. *Journal of Climate*, *17*(23), 4541–4563. doi: 10.1175/3222.1

Massie, S., Gettelman, A., Randel, W., & Baumgardner, D. (2002, 11). Distribution of tropical cirrus in relation to convection. *Journal of Geophysical Research: Atmospheres*, *107*(D21), 19–1. doi: 10.1029/2001JD001293

McFarquhar, G. M., & Heymsfield, A. J. (1996, 9). Microphysical Characteristics of Three Anvils Sampled during the Central Equatorial Pacific Experiment. *Journal of the Atmospheric Sciences*, *53*(17), 2401–2423. doi: 10.1175/1520-0469(1996)053⟨2401:MCOTAS⟩2.0.CO;2

McFarquhar, G. M., Heymsfield, A. J., Spinhirne, J., & Hart, B. (1999, 6). Thin and Subvisual Tropopause Tropical Cirrus: Observations and Radiative Impacts. *Journal of the Atmospheric Sciences*, *57*(12), 1841–1853. doi:

10.1175/1520-0469(2000)057⟨1841:TASTTC⟩2.0.CO;2

McGill, M. J., Vaughan, M. A., Trepte, C. R., Hart, W. D., Hlavka, D. L., Winker, D. M., & Kuehn, R. (2007, 10). Airborne validation of spatial properties measured by the CALIPSO lidar. *Journal of Geophysical Research*, *112*(D20), D20201. doi: 10.1029/2007JD008768

Mlawer, E. J., Taubman, S. J., Brown, P. D., Iacono, M. J., & Clough, S. A. (1997, 7). Radiative transfer for inhomogeneous atmospheres: RRTM, a validated correlated-k model for the longwave. *Journal of Geophysical Research: Atmospheres*, *102*(D14), 16663–16682. doi: 10.1029/97JD00237

Nesbitt, S. W., & Zipser, E. J. (2003, 5). The Diurnal Cycle of Rainfall and Convective Intensity according to Three Years of TRMM Measurements. *Journal of Climate*, *16*(10), 1456–1475. doi: 10.1175/1520-0442-16.10.1456

Ohno, T., Satoh, M., & Noda, A. (2019, 6). Fine Vertical Resolution RadiativeConvective Equilibrium Experiments: Roles of Turbulent Mixing on the HighCloud Response to Sea Surface Temperatures. *Journal of Advances in Modeling Earth Systems*, *11*(6), 1637–1654. doi: 10.1029/2019MS001704

Platnick, S., Meyer, K. G., King, M. D., Wind, G., Amarasinghe, N., Marchant, B., ... Riedi, J. (2017, 1). The MODIS Cloud Optical and Microphysical Products: Collection 6 Updates and Examples from Terra and Aqua. *IEEE Transactions on Geoscience and Remote Sensing*, *55*(1), 502–525. doi: 10.1109/TGRS.2016.2610522

Ramanathan, V., Cess, R. D., Harrison, E. F., Minnis, P., Barkstrom, B. R., Ahmad, E., & Hartmann, D. (1989). Cloud-radiative forcing and climate: Results from the earth radiation budget experiment. *Science*, *243*(4887), 57–63. doi: 10.1126/science.243.4887.57

Randall, D. A., Harshvardhan, Dazlich, D. A., & Corsetti, T. G. (1989). Interactions among radiation, convection, and large-scale dynamics in a general circulation model. *Journal of the Atmospheric Sciences*. doi: 10.1175/1520-0469(1989)046⟨1943:IARCAL⟩2.0.CO;2

Schmidt, C. T., & Garrett, T. J. (2013). A Simple Framework for the Dynamic Response of Cirrus Clouds to Local Diabatic Radiative Heating. *Journal of the Atmospheric Sciences*, *70*(5), 1409–1422. doi: 10.1175/JAS-D-12-056.1

Seeley, J. T., Jeevanjee, N., Langhans, W., & Romps, D. M. (2019, 1). Formation of Tropical Anvil Clouds by Slow Evaporation. *Geophysical Research Letters*, *46*(1), 492–501. doi: 10.1029/2018GL080747

Setvák, M., Rabin, R. M., & Wang, P. K. (2006). Contribution of the MODIS instrument to observations of deep convective storms and stratospheric moisture detection in GOES and MSG imagery. doi: 10.1016/j.atmosres.2005.09.015

Sourdeval, O., Gryspeerdt, E., Krämer, M., Goren, T., Delanoë, J., Afchine, A., ... Quaas, J. (2018). Ice crystal number concentration estimates from lidar-radar satellite remote sensing-Part 1: Method and evaluation. *Atmos. Chem. Phys*, *18*, 14327–14350. doi: 10.5194/acp-18-14327-2018

Stein, T. H. M., Delanoë, J., & Hogan, R. J. (2011, 9). A Comparison among Four Different Retrieval Methods for Ice-Cloud Properties Using Data from CloudSat , CALIPSO , and MODIS. *Journal of Applied Meteorology and Climatology*, *50*(9), 1952–1969. doi: 10.1175/2011JAMC2646.1

Stephens, G. L., Vane, D. G., Boain, R. J., Mace, G. G., Sassen, K., Wang, Z., ... Mitrescu, C. (2002, 12). The cloudsat mission and the A-Train: A new dimension of space-based observations of clouds and precipitation. *Bulletin of the American Meteorological Society*, *83*(12), 1771–1790. doi: 10.1175/BAMS-83-12-1771

Tompkins, A. M., & Craig, G. C. (1999). Sensitivity of tropical convection to sea surface temperature in the absence of large-scale flow. *Journal of Climate*. doi: 10.1175/1520-0442(1999)012⟨0462:SOTCTS⟩2.0.CO;2

Voigt, A., & Shaw, T. A. (2015). Circulation response to warming shaped by radiative changes of clouds and water vapour. *Nature Geoscience*. doi: 10.1038/ngeo2345

Wall, C. J., Hartmann, D. L., & Norris, J. R. (2019, 10). Is the net cloud radiative effect constrained to be uniform over the tropical warm pools? *Geophysical Research Letters*, 2019GL083642. doi: 10.1029/2019GL083642

Wall, C. J., Hartmann, D. L., Thieman, M. M., Smith, W. L., & Minnis, P. (2018, 12). The life cycle of anvil clouds and the top-of-atmosphere radiation balance over the tropical west Pacific. *Journal of Climate*, *31*(24), 10059–10080. doi: 10.1175/JCLI-D-18-0154.1

Wing, A. A., & Emanuel, K. A. (2014). Physical mechanisms controlling self-aggregation of convection in idealized numerical modeling simulations. *Journal of Advances in Modeling Earth Systems*. doi: 10.1002/2013MS000269

Winker, D. M., Pelon, J., Coakley, J. A., Ackerman, S. A., Charlson, R. J., Colarco, P. R., ... Wielicki, B. A. (2010, 3). The CALIPSO Mission. *Bulletin of the American Meteorological Society*, *91*(9), 1211–1230. doi: 10.1175/2010BAMS3009.1

Winker, D. M., & Trepte, C. R. (1998, 9). Laminar cirrus observed near the tropical tropopause by LITE. *Geophysical Research Letters*, *25*(17), 3351–3354. doi: 10.1029/98GL01292

Young, A. H., Bates, J. J., & Curry, J. A. (2012, 7). Complementary use of passive and active remote sensing for detection of penetrating convection from CloudSat, CALIPSO, and Aqua MODIS. *Journal of Geophysical Research: Atmospheres*, *117*(D13). doi: 10.1029/2011JD016749

Yuan, J., & Houze, R. A. (2010). Global variability of mesoscale convective system anvil structure from A-train satellite data. *Journal of Climate*, *23*(21), 5864–5888. doi: 10.1175/2010JCLI3671.1

Yuan, J., Houze, R. A., & Heymsfield, A. J. (2011). Vertical structures of anvil clouds of tropical mesoscale convective systems observed by CloudSat. *Journal of the Atmospheric Sciences*, *68*(8), 1653–1674. doi: 10.1175/2011JAS3687.1

Zelinka, M. D., & Hartmann, D. L. (2010). Why is longwave cloud feedback positive? *Journal of Geophysical Research Atmospheres*, *115*(16). doi: 10.1029/2010JD013817

Figure 1.

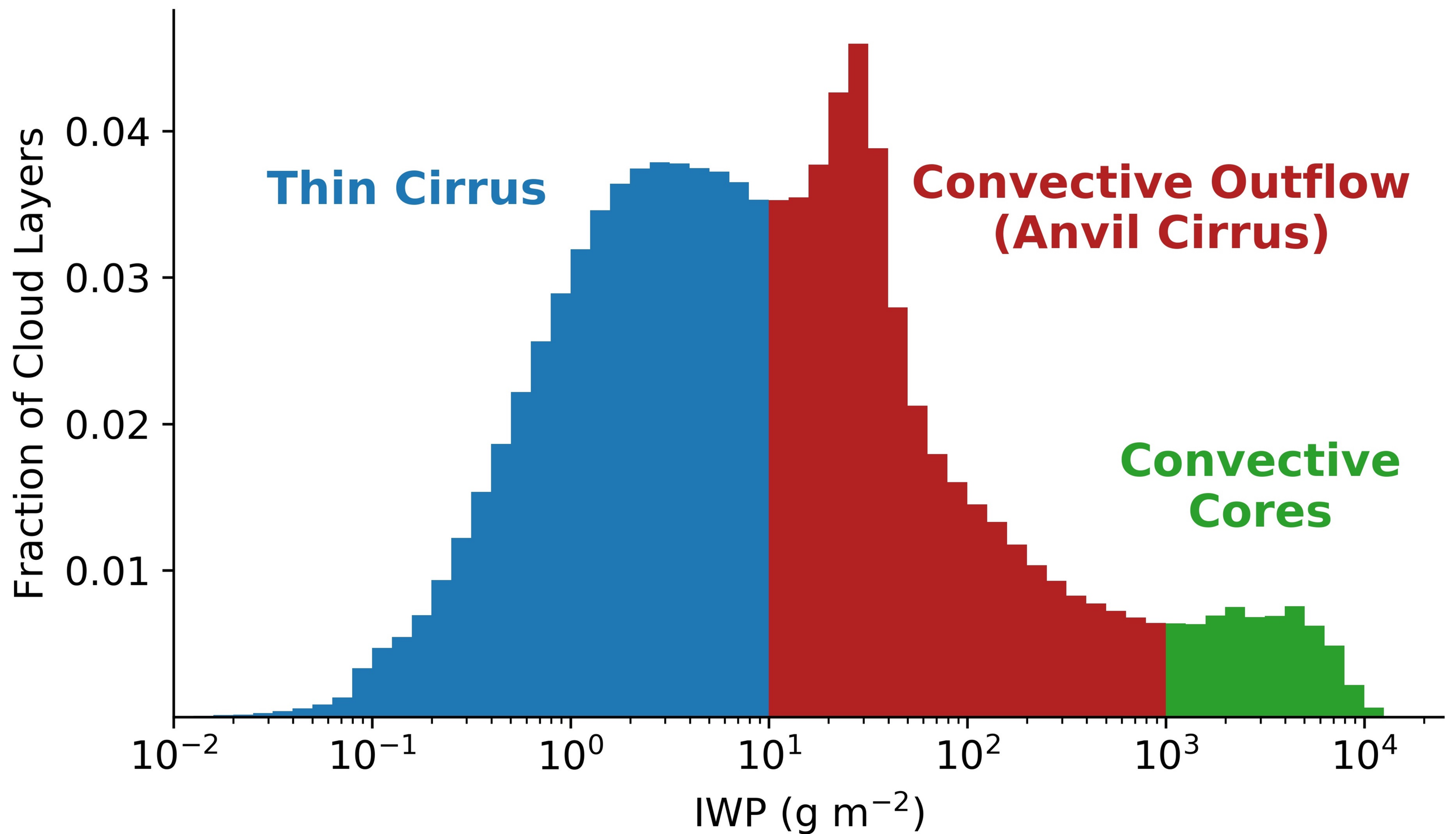
Thin Cirrus
Convective Outflow
(Anvil Cirrus)
Convective
Cores
Fraction of Cloud Layers
0.04
0.03
0.02
0.01
10^{-2}
10^{-1}
10^{0}
10^{1}
10^{2}
10^{3}
10^{4}
IWP (g m^{-2})

Figure 2.

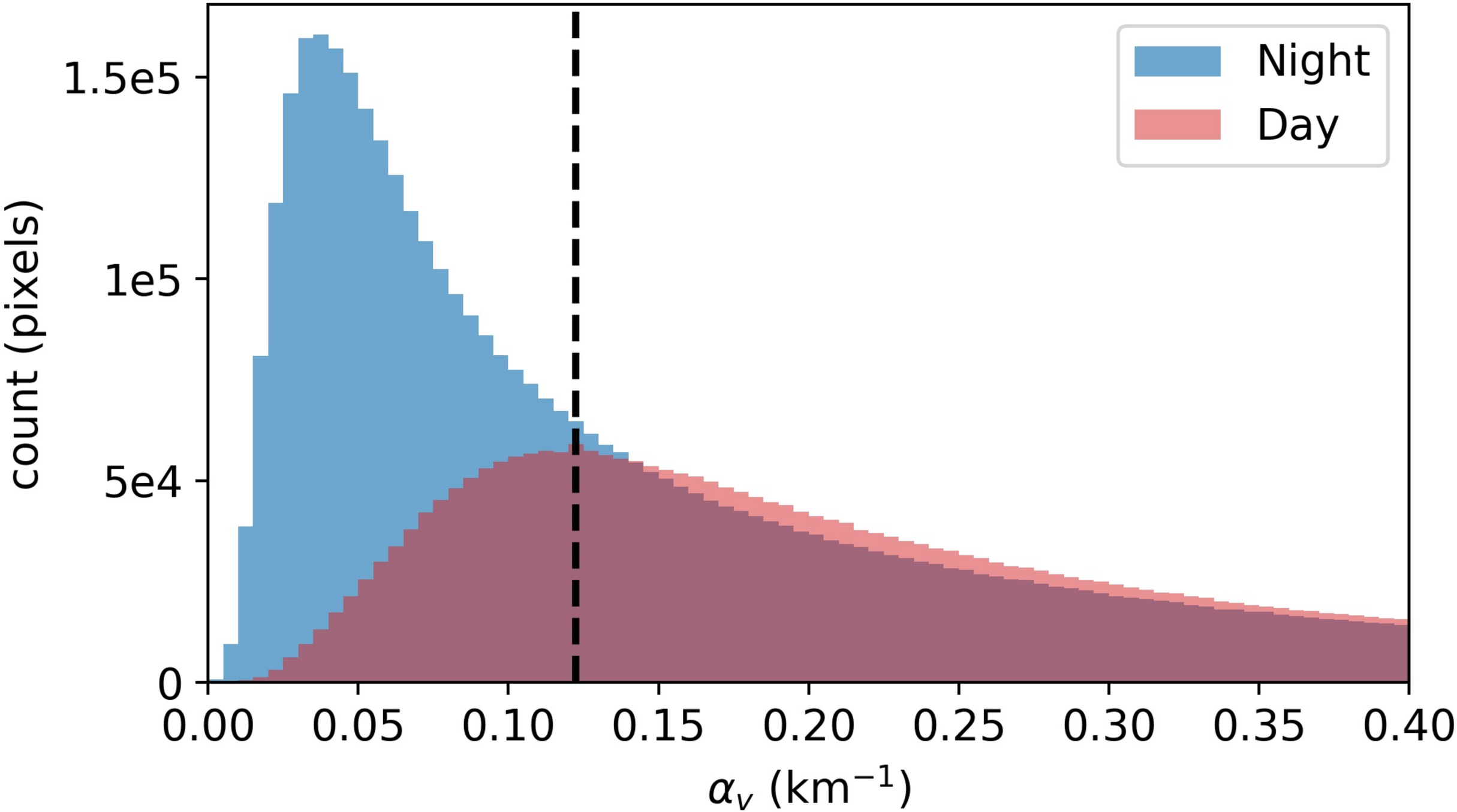
Night
Day
count (pixels)
1.5e5
1e5
5e4
0
0.00
0.05
0.10
0.15
0.20
0.25
0.30
0.35
0.40
α_v (km^{-1})

Figure 3.

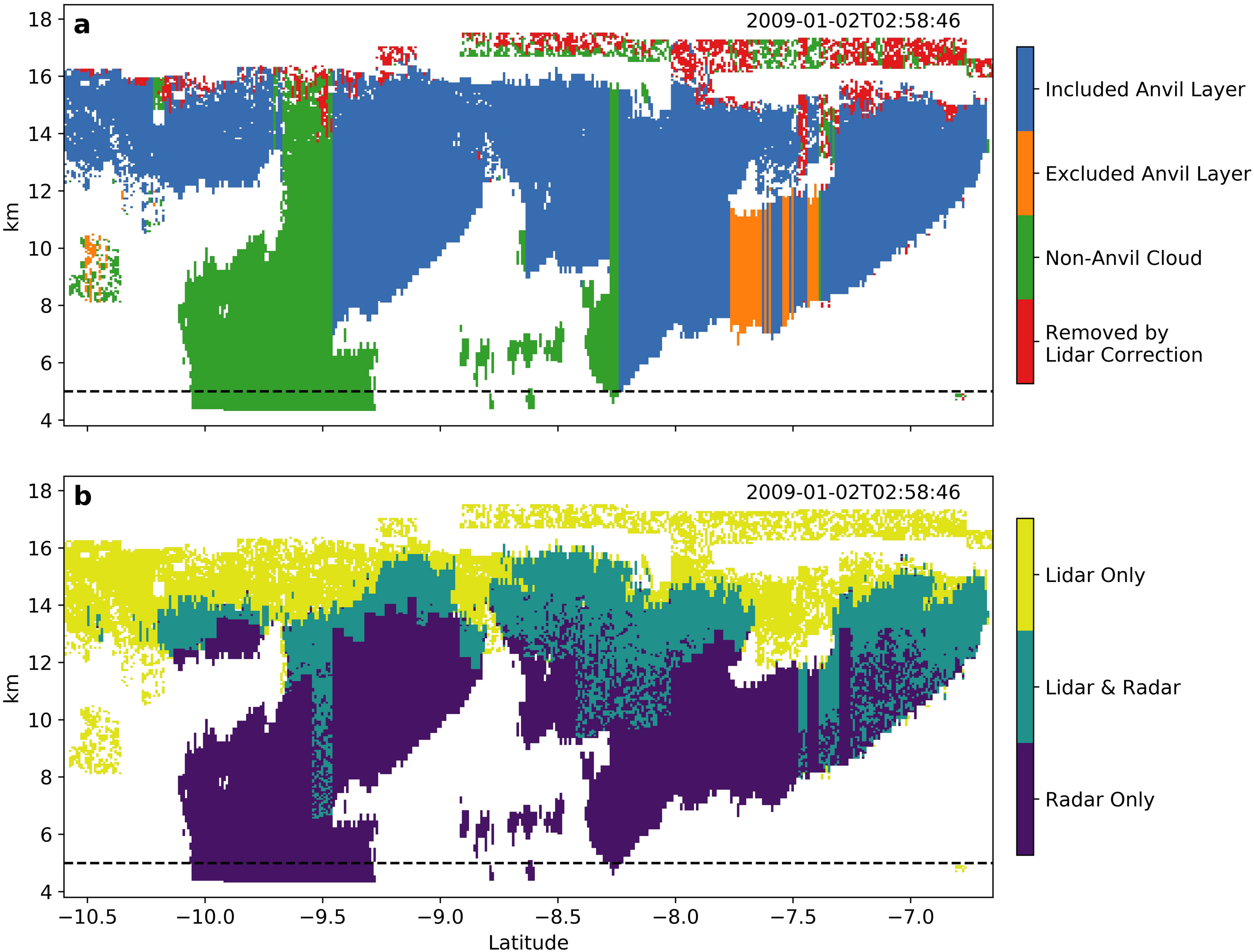
a
2009-01-02T02:58:46
Included Anvil Layer
Excluded Anvil Layer
Non-Anvil Cloud
Removed by
Lidar Correction
b
2009-01-02T02:58:46
Lidar Only
Lidar & Radar
Radar Only
km
18
16
14
12
10
8
6
4
−10.5
−10.0
−9.5
−9.0
−8.5
−8.0
−7.5
−7.0
Latitude

Figure 4.

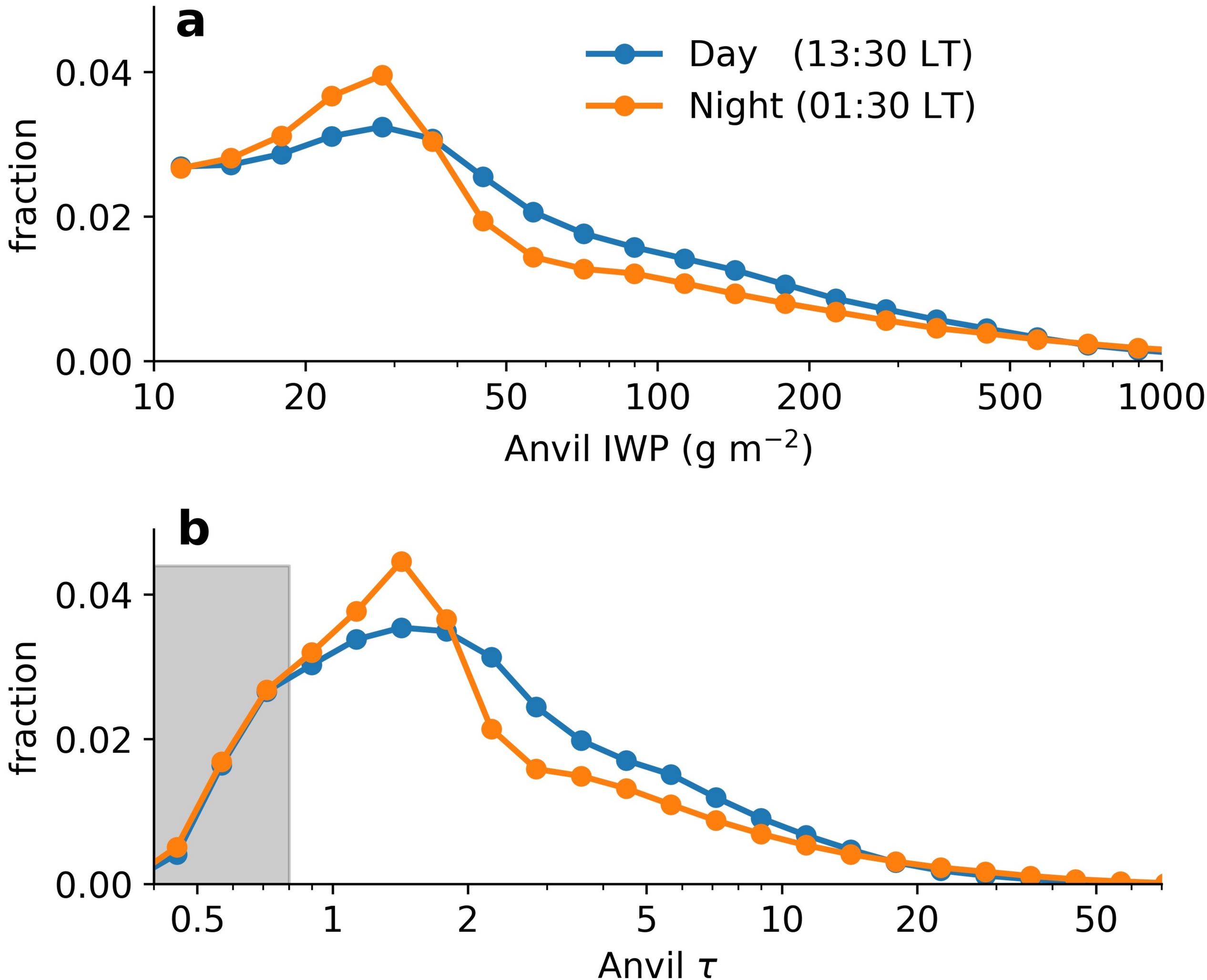
a
Day (13:30 LT)
Night (01:30 LT)
fraction
0.04
0.02
0.00
10
20
50
100
200
500
1000
Anvil IWP (g m^{-2})
b
fraction
0.04
0.02
0.00
0.5
1
2
5
10
20
50
Anvil τ

Figure 5.

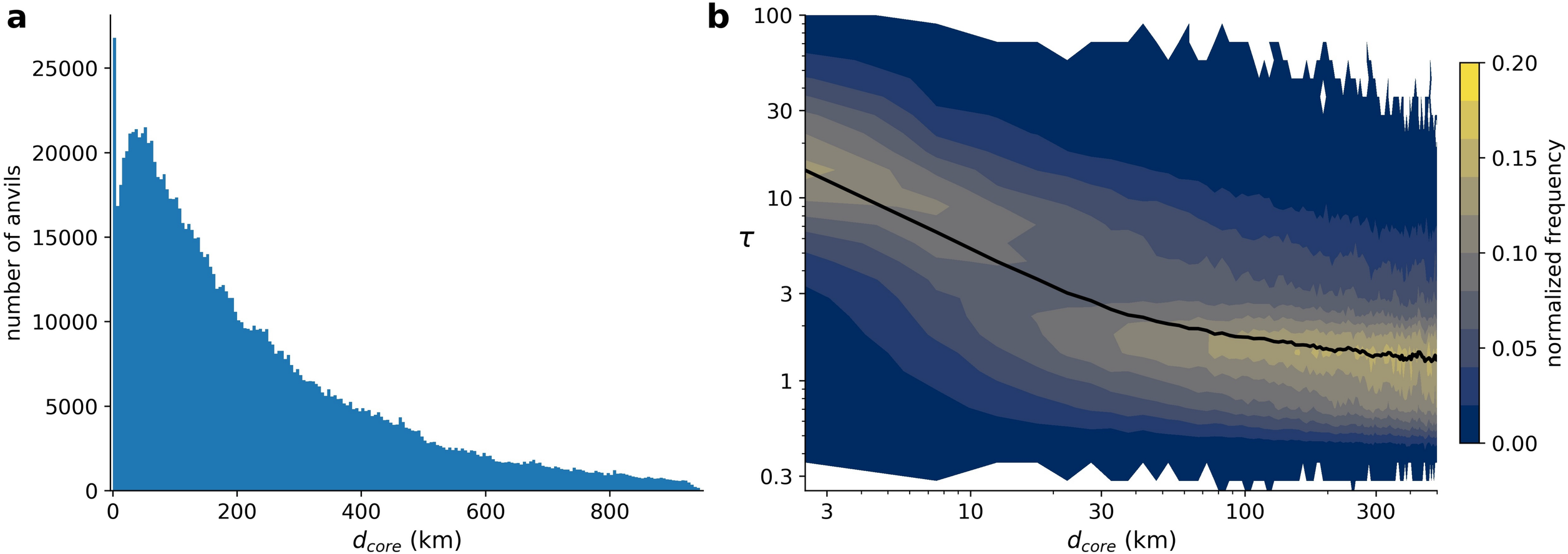
a
number of anvils
25000
20000
15000
10000
5000
0
0
200
400
600
800
d_{core} (km)
b
τ
100
30
10
3
1
0.3
3
10
30
100
300
d_{core} (km)
normalized frequency
0.20
0.15
0.10
0.05
0.00

Figure 6.

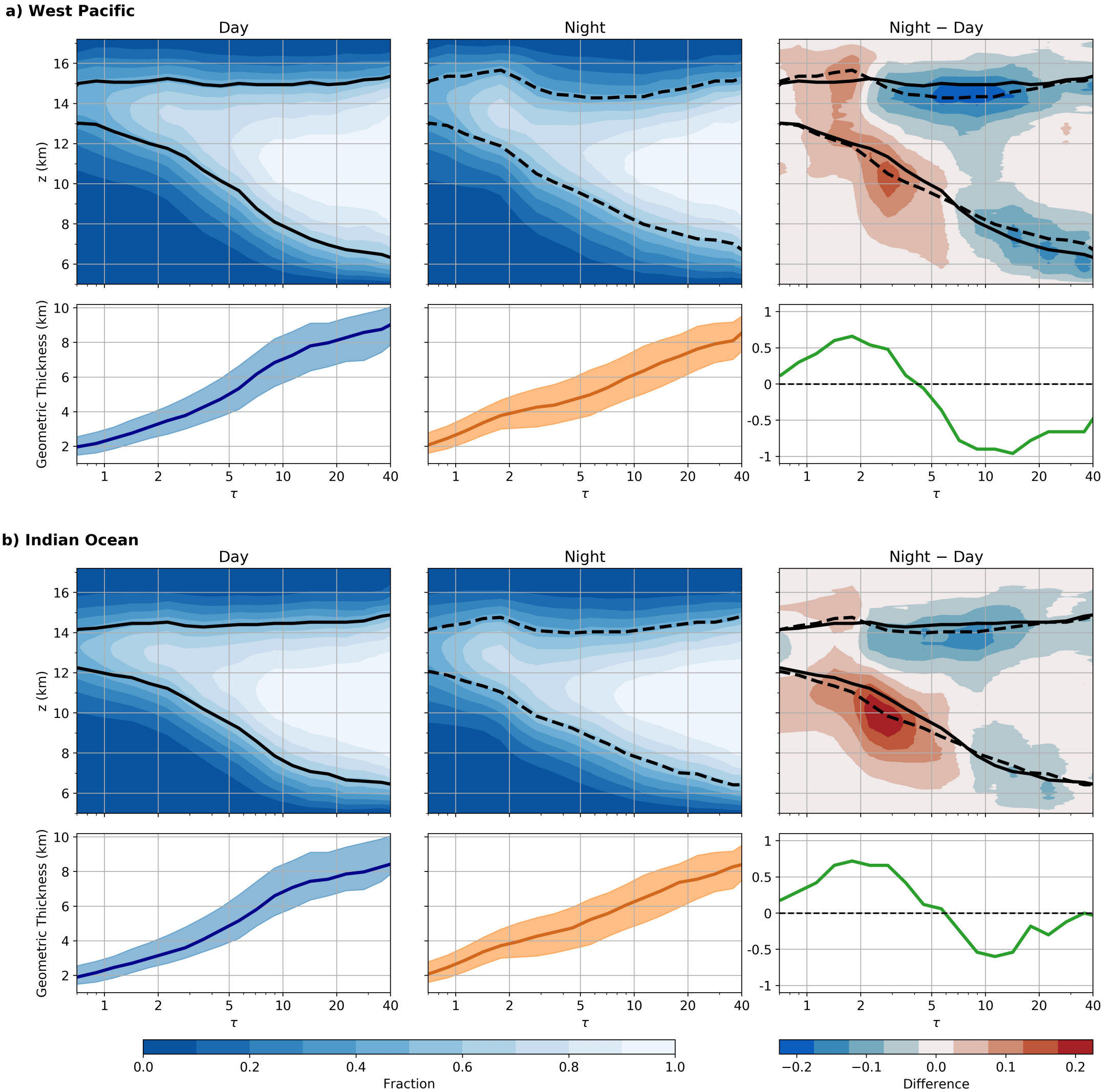
a) West Pacific
Day
Night
Night − Day
z (km)
Geometric Thickness (km)
τ
b) Indian Ocean
Day
Night
Night − Day
z (km)
Geometric Thickness (km)
τ
Fraction
Difference

Figure 7.

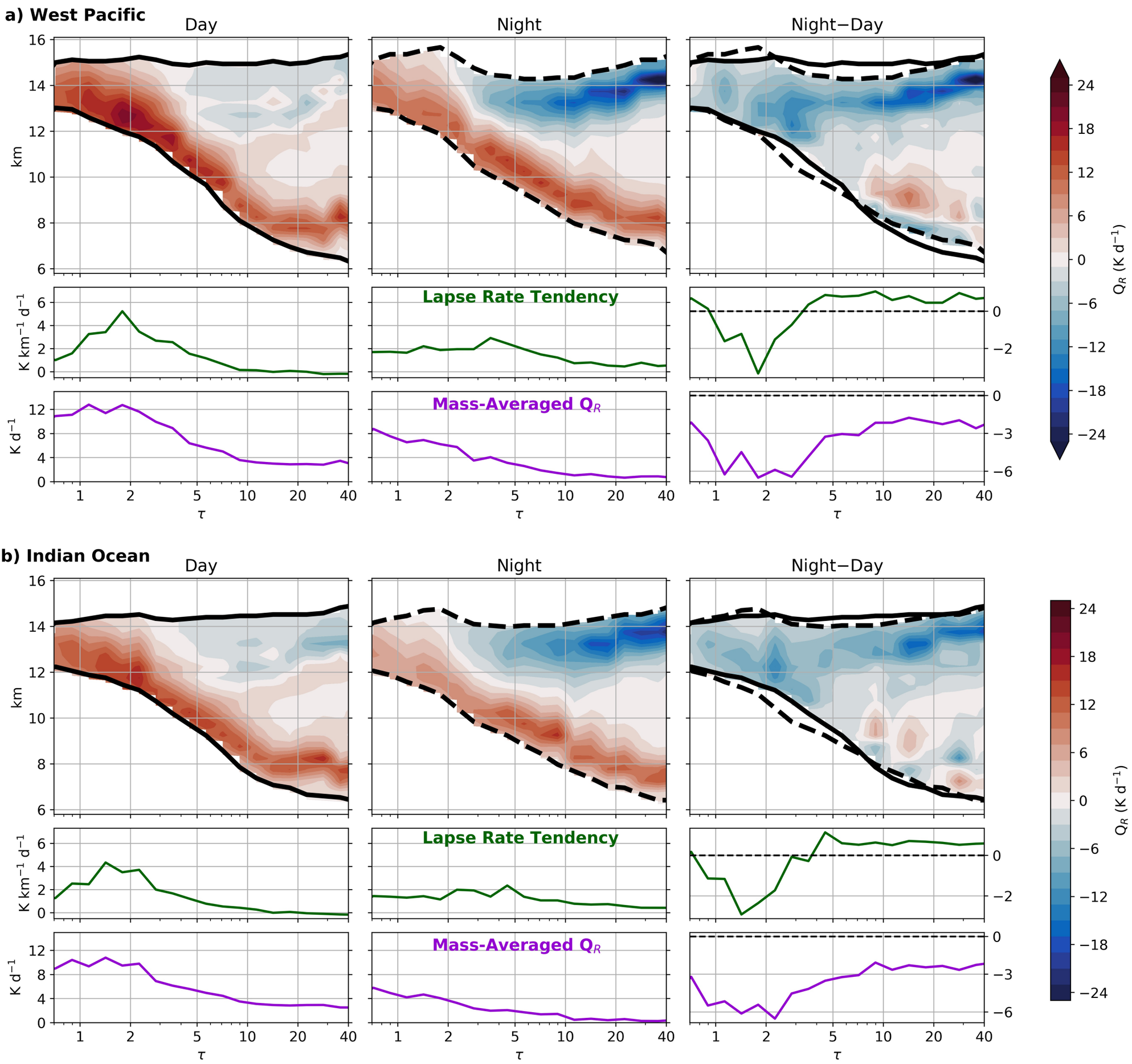
a) West Pacific
Day
Night
Night−Day
km
Lapse Rate Tendency
K km^{-1} d^{-1}
Mass-Averaged Q_R
K d^{-1}
τ
Q_R (K d^{-1})
b) Indian Ocean
Day
Night
Night−Day
km
Lapse Rate Tendency
K km^{-1} d^{-1}
Mass-Averaged Q_R
K d^{-1}
τ
Q_R (K d^{-1})

Figure 8.

a) Ice Crystal Effective Radius

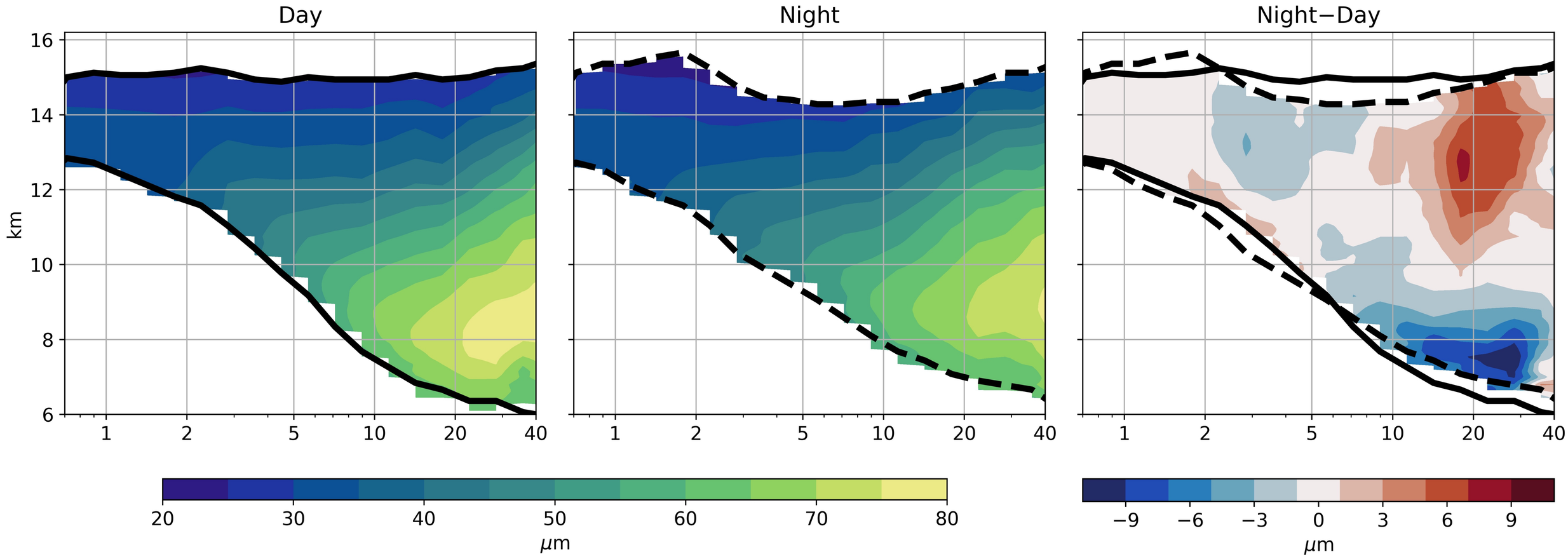

b) Ice Crystal Number Concentration (>5 μm)

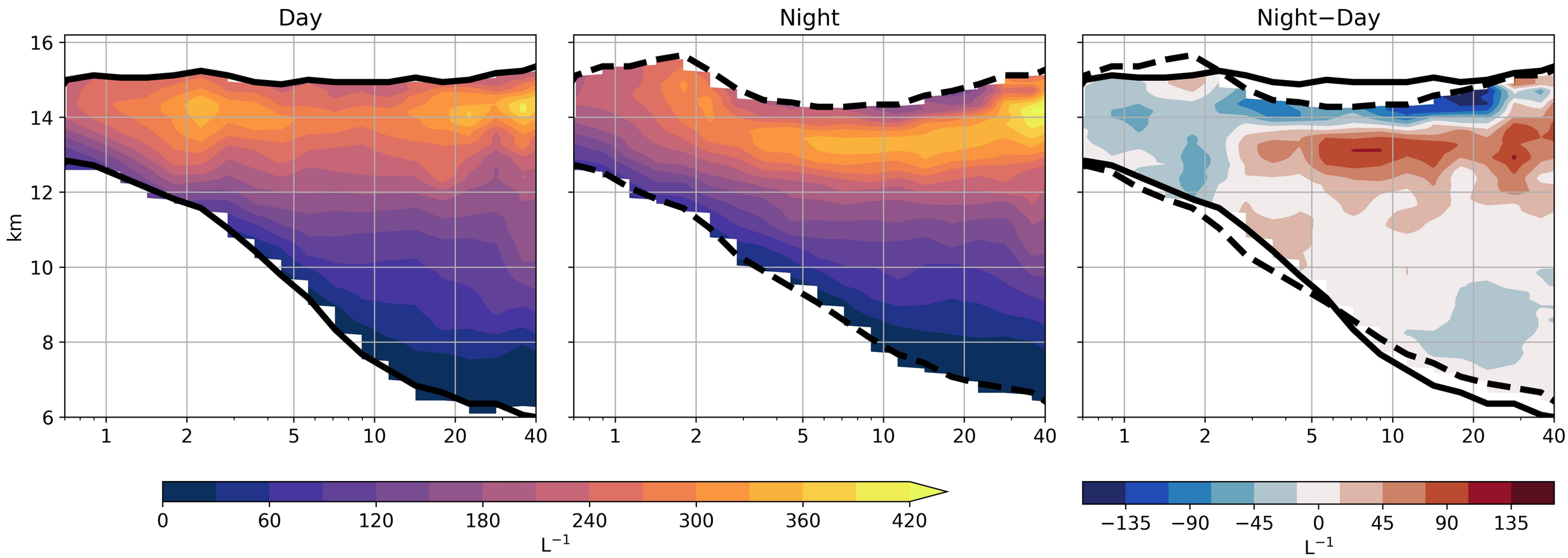

c) Ice Water Content

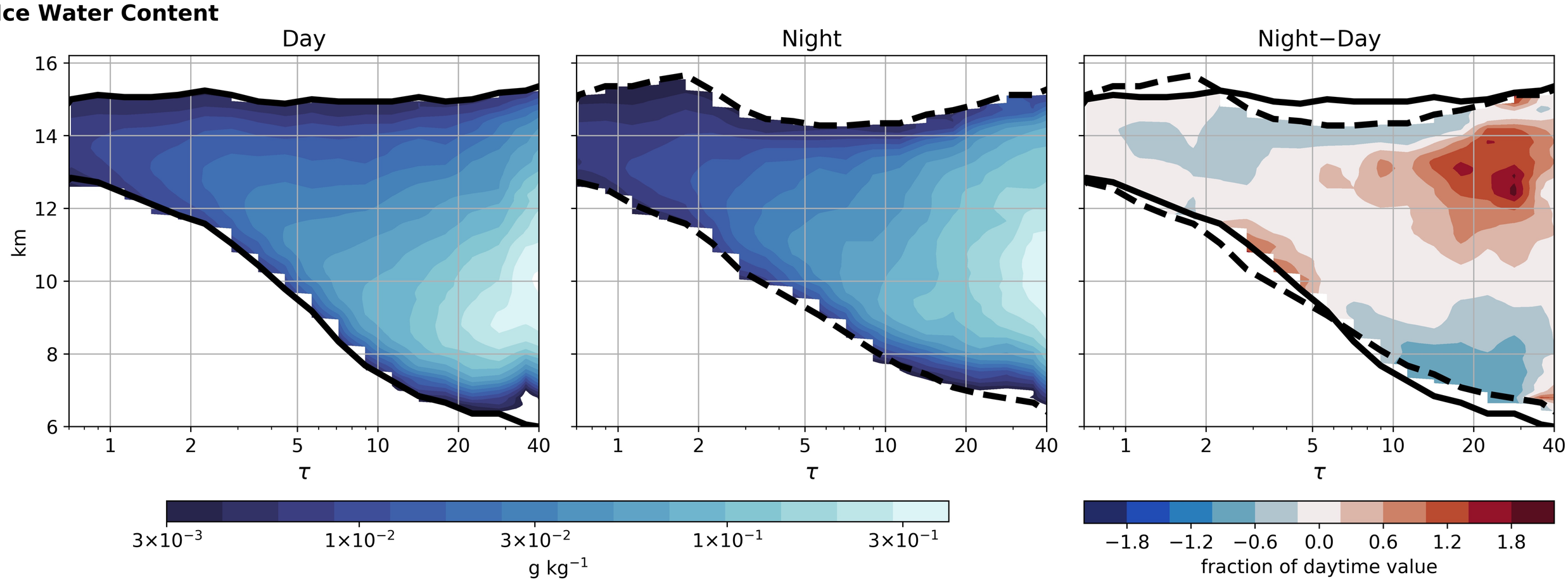

Figure 9.

a) Ice Crystal Effective Radius

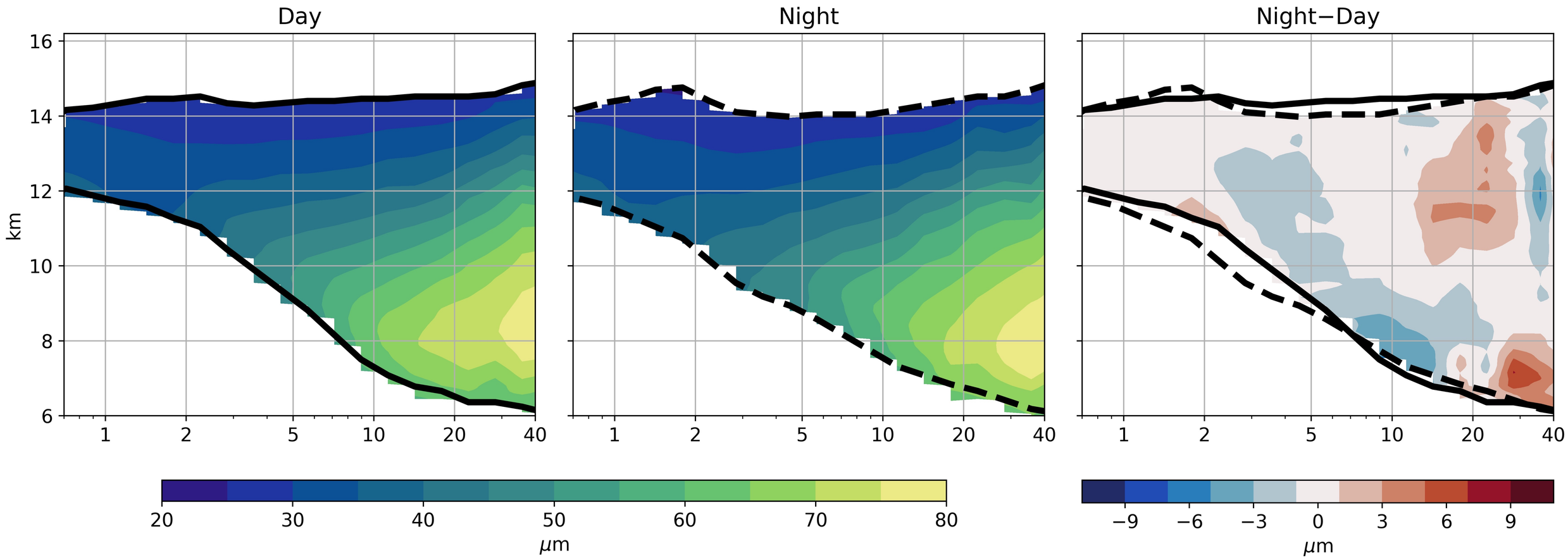

b) Ice Crystal Number Concentration (>5 μm)

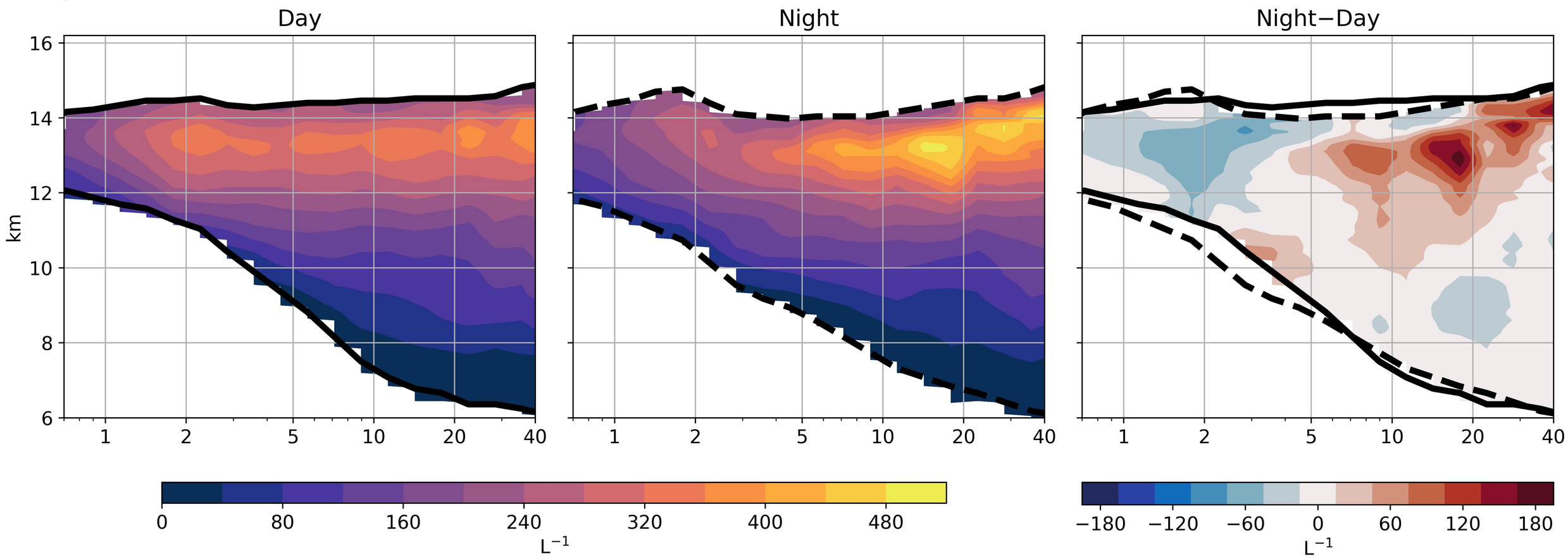
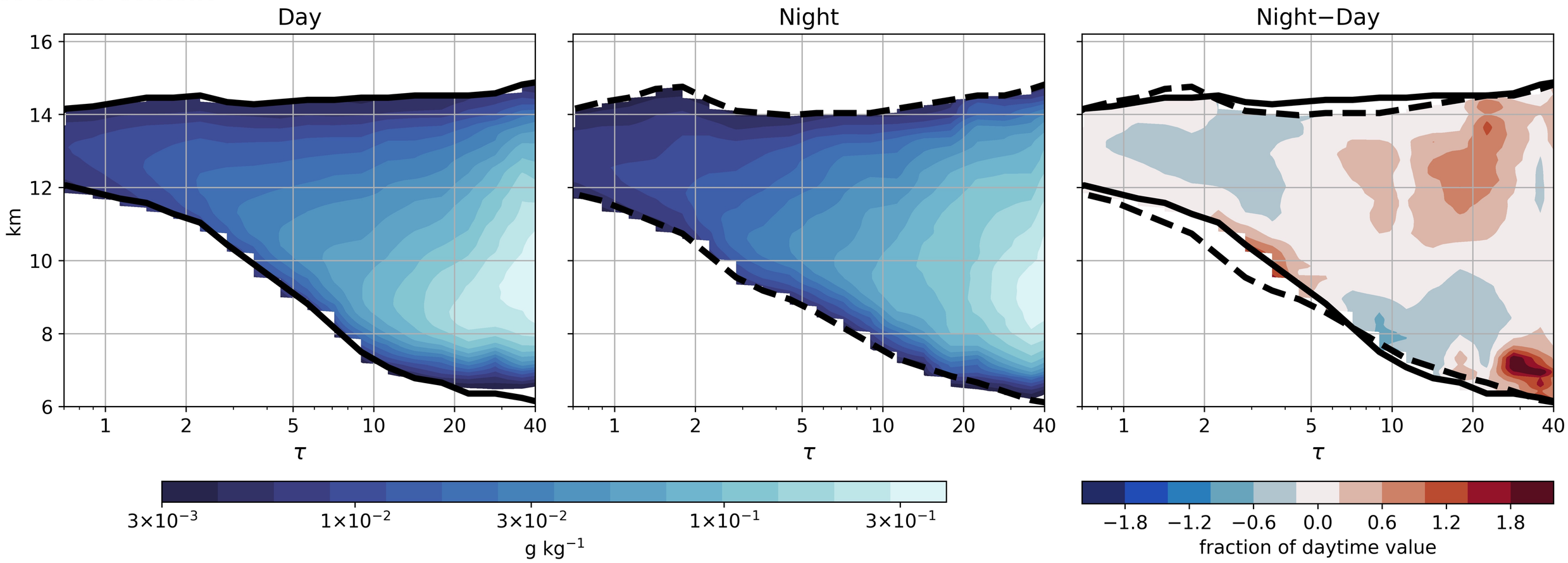
c) Ice Water Content